PHYSICAL REVIEW A **99**, 053405 (2019)

Inclusion of Coulomb effects in laser-atom interactions

J. Dubois,[1] S. A. Berman,[1,2,*] C. Chandre,[1] and T. Uzer[2]
[1] *Aix Marseille Univ, CNRS, Centrale Marseille, I2M, Marseille, France*
[2] *School of Physics, Georgia Institute of Technology, Atlanta, Georgia 30332-0430, USA*

(Received 4 February 2019; published 6 May 2019)

We investigate the role of the Coulomb interaction in strong field processes. We find that the Coulomb field of the ion makes its presence known even in highly intense laser fields, in contrast to the assumptions of the strong field approximation. The dynamics of the electron after ionization is analyzed with four models for an arbitrary laser polarization: the Hamiltonian model in the dipole approximation, the strong field approximation, the Coulomb-corrected strong field approximation, and the guiding center. These models illustrate clearly the Coulomb effects, in particular Coulomb focusing and Coulomb asymmetry. We show that the Coulomb-corrected strong field approximation and the guiding center are complementary, in the sense that the Coulomb-corrected strong field approximation describes well short timescale phenomena (shorter than a laser cycle) for which the Coulomb interaction is significant on short timescales, such as in subcycle recollisions, while the guiding center is well suited for describing long timescale phenomena (longer than a laser cycle) for which the Coulomb interaction is significant on long timescales, such as in Coulomb-driven recollisions and Rydberg state creation.

DOI: 10.1103/PhysRevA.99.053405

I. INTRODUCTION

After ionization in an intense laser field, an ionized electron travels in the continuum until it reaches the detector, or it can come back to the ionic core and probe the target in a process called recollision. Recollisions are key processes in attosecond physics [1–6], since they are the origin of a variety of highly nonlinear phenomena, such as high harmonic generation (HHG), nonsequential double ionization (NSDI), and above-threshold ionization (ATI). Such processes are widely used in attosecond physics in order to obtain information about the target atoms or molecules. For example, it is possible to perform imaging of molecular orbitals [7–9] and determine the electronic dynamics inside atoms or molecules [10,11]. Historically, the first model of the recollision scenario makes use of the so-called strong field approximation (SFA), where the effects of the Coulomb interaction after tunnel ionization are neglected [12]. The recollision scenario [1,13] based on the SFA has three steps: (i) The electron tunnel ionizes through the barrier induced by the laser field on the ionic core potential [12,14], (ii) travels in the laser field alone, and then upon return to the ionic core, and (iii) recombines with the ion (and triggers HHG), or rescatters from the ionic core, either elastically (ATI) or inelastically (NSDI).

In step (ii) of the recollision scenario, the electrons are outside the ionic core region, in the continuum, and their dynamics is mainly classical. The main advantage of the use of the SFA in step (ii) is the analytic expressions of the trajectories, which sheds some light on the recollision process. In some cases, the SFA encounters success, for instance for predicting the HHG cutoff [1,15] or frequency versus time profile of HHG radiation [16]. In other cases, the SFA is inaccurate when it is confronted with experimental results [17–19], especially when long timescale trajectories (of the order of multiple laser periods) are involved in the experiment. In linearly polarized (LP) fields, the SFA suggests that if the electron does not return to the ionic core in less than one laser cycle after ionization, it never comes back to the core (or with very low probability). However, recollisions involving multiple laser cycles have a significant effect in NSDI. Including the Coulomb interaction increases the NSDI probability (i.e., the recollision probability) by about one order of magnitude [19–22]. Coulomb effects play a significant role in ATI experiments as well [17,18,23].

Here we investigate the role of the Coulomb interaction in the recollision and ionization processes by shuttling between four models, namely: the Hamiltonian in the dipole approximation (referred to as the reference Hamiltonian) which combines both the laser and the Coulomb interaction, the SFA, the Coulomb-corrected SFA [17] (CCSFA), and the guiding-center (GC) model [24,25]. Here the SFA and the CCSFA are referred to as their fully classical interpretation for step (ii) of the recollision process. The classical version of SFA and CCSFA is the backbone of more elaborated SFA and CCSFA theories which take into account semiclassical and quantum effects [15]. The SFA, which ignores the Coulomb interaction, is used to point out the contributions of the Coulomb potential in the reference model. The CCSFA and GC models decouple the laser and Coulomb interactions through perturbation theory and averaging, respectively, and they are used to analyze the contributions of each interaction independently. We show that the CCSFA and GC models are complementary, in the sense that CCSFA describes well short timescale phenomena (shorter than a laser cycle) for which the Coulomb interaction is significant for short times, while the GC is well suited for describing long timescale phenomena (longer than a laser

---

[*] Present address: School of Natural Sciences, University of California, Merced, Merced, California 95343, USA.

cycle) for which the Coulomb interaction is significant for long times, such as in multiple laser cycle recollisions, which we refer to as Coulomb-driven recollisions.

In particular, in photoelectron momentum distributions (PMDs), there is an asymmetry with respect to the minor polarization axis, known as the Coulomb asymmetry [17], and a decrease of the final electron energy, referred to as Coulomb focusing [19,26]. In Ref. [24] we introduced the GC model for the motion of ionized electrons, and we used it to identify the mechanism behind the bifurcation in the peak of the PMDs as a function of the ellipticity observed in experiments [18,27]. This bifurcation was attributed as a clear signature of the Coulomb effects. There we also showed that the mechanism behind the bifurcation is closely related to Rydberg state creation [28], a process that cannot be described without the Coulomb interaction. In this article, on the one hand, we show that the GC model can also be used to quantify the amount of Rydberg state creation and to demonstrate their close relation with the Coulomb-driven recollisions. On the other hand, we show that the Coulomb interaction makes its presence known for long timescale phenomena such as ATI, in particular the Coulomb asymmetry, even at high intensity when the assumptions of the SFA are met.

The article is organized as follows: In Sec. II we describe step (i) coupled with step (ii) of the recollision scenario, using the reference Hamiltonian and the three reduced models (SFA, CCSFA, and GC models) we employ throughout the article. In Sec. III we analyze the PMDs and the initial conditions leading to the PMDs with the four models. In particular, we identify the set of initial conditions leading to Rydberg state creation and Coulomb-driven recollisions. We show that these processes are only well described by the GC model. In Sec. IV we use the GC model to describe the mechanisms behind Rydberg state creation and Coulomb-driven recollisions. In particular, the GC model allows us to define a domain of initial conditions, which we refer to as the rescattering domain, leading to Rydberg state creation and Coulomb-driven recollisions. Finally, in Sec. V we investigate the shape of the rescattering domain using the GC model. We show how the shape and location of the rescattering domain manifests itself in experiments, in particular, in the bifurcation of the PMDs [24].

II. THE MODELS

First, we describe the reference model: The atom is described with a single active electron, the ionic core is set at the origin and is assumed to be static. The position of the electron is denoted $\mathbf{r}$, and its conjugate momentum is $\mathbf{p}$. In the length gauge [9] and the dipole approximation, the Hamiltonian governing the dynamics of an electron in an atom driven by a laser field reads

$$H(\mathbf{r},\mathbf{p},t)=\frac{|\mathbf{p}|^2}{2}+V(\mathbf{r})+\mathbf{r}\cdot\mathbf{E}(t), \tag{1}$$

where atomic units (a.u.) are used unless stated otherwise. We use the soft-Coulomb potential [29] to describe the ion-electron interaction $V(\mathbf{r})=-(|\mathbf{r}|^2+1)^{-1/2}$. The electric field is elliptically polarized,

$$\mathbf{E}(t)=\frac{E_0 f(t)}{\sqrt{\xi^2+1}}[\hat{\mathbf{x}}\cos(\omega t)+\hat{\mathbf{y}}\xi\sin(\omega t)].$$

The laser frequency we use is $\omega=0.0584$ a.u. (corresponding to infrared light of wavelength 780 nm), the laser ellipticity is $\xi\in[0,1]$, and the laser amplitude is $E_0=5.338\times10^{-9}\sqrt{I}$ with I the intensity in W cm^{-2}. The laser envelope $f(t)$ is such that $f(t)=1$ for $t\in[0,T_p]$, $f(t)=(T_f-t)/(T_f-T_p)$ for $t\in[T_p,T_f]$, and $f(t)=0$ otherwise. Here T_p and T_f are the duration of the plateau and the laser pulse, respectively. Throughout the article we use a two laser cycle ramp down, i.e., $T_f=T_p+2T$, where $T=2\pi/\omega$ is the laser period. The duration of the plateau is $T_p=8T$ unless stated otherwise. The major and minor polarization axes are $\hat{\mathbf{x}}$ and $\hat{\mathbf{y}}$, respectively.

A. Step (i): Ionization model

When the laser field starts to oscillate, it creates an effective potential barrier through which the electron can tunnel ionize. We use the Perelomov-Popov-Terent'ev (PPT) [30–32] theory to define the ionization rate and the initial conditions after ionization. The Keldysh parameter [12] $\gamma=\omega\sqrt{2I_p}/E_0$, where I_p is the ionization potential, is used to estimate the dominant ionization process. If $\gamma\ll1$, the ionization process is the adiabatic tunnel ionization [12,14], i.e., the potential barrier is quasistatic during the tunneling. If $\gamma\gg1$, the dominant process is multiphoton absorption. For $\gamma\sim1$, the process is in between tunnel ionization and multiphoton absorption. During this so-called nonadiabatic tunnel ionization [30–32], the wave packet absorbs photons during the tunneling [33]. Here we show a brief summary of the PPT theory [30–32] used in this article for the ionization rate and the initial conditions of the electron after ionization.

The initial conditions and the ionization rate of the electron are parametrized by the ionization time t_0 and its momentum $\mathbf{p}_0$ at t_0. The ionization rate $W(t_0,\mathbf{p}_0)$ is given in Eq. (A1) while the initial conditions at $t=t_0$ of the electron are

$$\mathbf{r}_0=\frac{|\mathbf{E}(t_0)|}{\omega^2}(1-\cosh\tau_0)\hat{\mathbf{n}}_{\parallel}(t_0), \tag{2a}$$

$$\mathbf{p}_0=p_{\parallel}\hat{\mathbf{n}}_{\parallel}(t_0)+p_{\perp}\hat{\mathbf{n}}_{\perp}(t_0)+p_{z,0}\hat{\mathbf{z}}, \tag{2b}$$

with $\hat{\mathbf{n}}_{\parallel}(t_0)=\mathbf{E}(t_0)/|\mathbf{E}(t_0)|$ and $\hat{\mathbf{n}}_{\perp}(t_0)=-[\hat{\mathbf{n}}_{\parallel}(t_0)\cdot\hat{\mathbf{y}}]\hat{\mathbf{x}}+[\hat{\mathbf{n}}_{\parallel}(t_0)\cdot\hat{\mathbf{x}}]\hat{\mathbf{y}}$. In other words, $p_{\parallel}$ is the initial momentum of the electron along the electric field direction, $p_{\perp}$ is the initial momentum transverse to the electric field direction, and $p_{z,0}$ is the initial momentum perpendicular to the polarization plane $(\hat{\mathbf{x}},\hat{\mathbf{y}})$. The time $\tau_0=\tau_0(t_0)$ is the solution of the transcendental equation

$$\sinh^2\tau_0-\xi^2\left(\cosh\tau_0-\frac{\sinh\tau_0}{\tau_0}\right)^2=\gamma_0(t_0)^2, \tag{3}$$

where $\gamma_0(t_0)=\omega\sqrt{2I_p}/|\mathbf{E}(t_0)|$. We consider He $(I_p=0.9)$ unless stated otherwise. According to the PPT ionization rate, the most probable trajectory ionizes at times $\omega t_0=n\pi$ (see Appendix A), i.e., at the peak amplitude of the electric field, where $n\in\mathbb{N}$, with initial longitudinal, transverse and perpendicular momenta

$$P_\parallel = 0, \tag{4a}$$

$$P_\perp = \frac{\xi E_0}{\omega\sqrt{\xi^2+1}}\left(1 - \frac{\sinh\tau}{\tau}\right), \tag{4b}$$

$$P_{z,0} = 0, \tag{4c}$$

respectively, with τ the solution of Eq. (3) for $\gamma_0(t_0) = \gamma\sqrt{\xi^2+1}$. We refer to the trajectory with initial conditions ($t_0 = T/2$, $p_\parallel = P_\parallel$, $p_\perp = P_\perp$, $p_{z,0} = P_{z,0}$) as the T trajectory. Hence, the T trajectory captures the dominant behavior of the ionized electrons. Moreover, it corresponds to a local maximum of the ionization rate for linearly and elliptically polarized pulses.

B. Step (ii): Classical models

1. *Reference Hamiltonian*

The reference Hamiltonian is defined in Eq. (1) with initial conditions $(\mathbf{r}_0, \mathbf{p}_0, t_0)$ given by Eq. (2). In order to derive the reduced models, we use a new set of phase-space coordinates $(\mathbf{r}_g, \mathbf{p}_g)$ such that

$$\mathbf{r}_g = \mathbf{r} - \boldsymbol{\Sigma}(t)/\omega^2, \tag{5a}$$

$$\mathbf{p}_g = \mathbf{p} - \mathbf{A}(t), \tag{5b}$$

where $\omega^2\mathbf{A}(t) = \partial\boldsymbol{\Sigma}(t)/\partial t$ and the vector potential $\mathbf{A}(t)$ is such that $\mathbf{E}(t) = -\partial\mathbf{A}(t)/\partial t$. Using integration by parts, $\mathbf{A}(t) = -f(t)E_0[\hat{\mathbf{x}}\sin(\omega t) - \xi\hat{\mathbf{y}}\cos(\omega t)]/\omega\sqrt{\xi^2+1} + O(T/T_f)$, where the terms of order $O(T/T_f)$ are due to the envelope variations. In the same way, $\boldsymbol{\Sigma}(t) = \mathbf{E}(t) + O(T/T_f)$. Here we mainly focus on the analyses of the electronic dynamics during the plateau, and we consider $\mathbf{A}(t) \approx -f(t)E_0[\hat{\mathbf{x}}\sin(\omega t) - \xi\hat{\mathbf{y}}\cos(\omega t)]/\omega\sqrt{\xi^2+1}$ and $\boldsymbol{\Sigma}(t) \approx \mathbf{E}(t)$.

Under the canonical change of coordinates (5), Hamiltonian (1) becomes

$$H_g(\mathbf{r}_g, \mathbf{p}_g, t) = \frac{|\mathbf{p}_g|^2}{2} + V[\mathbf{r}_g + \boldsymbol{\Sigma}(t)/\omega^2]. \tag{6}$$

The initial conditions in the new coordinates at time t_0, denoted $(\mathbf{r}_{g,0}, \mathbf{p}_{g,0})$, are related to the old coordinates by the transformation (5) and such that

$$\mathbf{r}_{g,0} = \mathbf{r}_0 - \boldsymbol{\Sigma}(t_0)/\omega^2, \tag{7a}$$

$$\mathbf{p}_{g,0} = \mathbf{p}_0 - \mathbf{A}(t_0). \tag{7b}$$

The dynamics described by Hamiltonians (1) and (6) are equivalent. In order to emphasize the role of the Coulomb interaction, we consider three reduced models in the new system of coordinates: the SFA where the Coulomb potential is neglected ($V = 0$), the CCSFA [17] where the Coulomb potential is assumed to be a perturbation of the SFA prediction, and the GC model [24,25] in which the electron trajectory is averaged over one laser cycle.

2. *SFA*

For the SFA and the CCSFA, we assume that the contribution of the Coulomb interaction on the electron dynamics acts on short timescales. Under this assumption, we write the Hamiltonian as

$$H_g(\mathbf{r}_g, \mathbf{p}_g, t) = \frac{|\mathbf{p}_g|^2}{2} + \epsilon V[\mathbf{r}_g + \boldsymbol{\Sigma}(t)/\omega^2],$$

where we have introduced an ordering parameter ϵ for bookkeeping purposes. The equations of motion of the electron are

$$\dot{\mathbf{r}}_g = \mathbf{p}_g, \quad \dot{\mathbf{p}}_g = -\epsilon\nabla V[\mathbf{r}_g + \boldsymbol{\Sigma}(t)/\omega^2].$$

We consider the correction due to the Coulomb interaction on a short timescale, hence $\mathbf{r}_g = \mathbf{r}_g^{\text{SFA}} + \epsilon\Delta\mathbf{r}_g + O(\epsilon^2)$ and $\mathbf{p}_g = \mathbf{p}_g^{\text{SFA}} + \epsilon\Delta\mathbf{p}_g + O(\epsilon^2)$. We substitute these equations in the equations of motion and we identify each terms by order of ϵ. The lowest order in ϵ provides the SFA electron phase-space trajectory

$$\mathbf{r}_g^{\text{SFA}}(t) = \mathbf{r}_{g,0} + \mathbf{p}_{g,0}(t - t_0), \tag{8a}$$

$$\mathbf{p}_g^{\text{SFA}}(t) = \mathbf{p}_{g,0}. \tag{8b}$$

The electron trajectory, in this new set of coordinates, is that of a free particle with constant energy and drift momentum $\mathcal{E}^{\text{SFA}} = |\mathbf{p}_g^{\text{SFA}}|^2/2$ and $\mathbf{p}_g^{\text{SFA}}$, respectively. At any time t, the position and momentum of the electron are obtained by inverting the change of coordinates (5).

3. *Coulomb-corrected SFA*

The first order in ϵ provides the correction due to the Coulomb interaction on the SFA trajectory, which reads

$$\Delta\mathbf{r}_g(t) = \int_{t_0}^{t} \Delta\mathbf{p}_g(s)\, ds, \tag{9a}$$

$$\Delta\mathbf{p}_g(t) = -\int_{t_0}^{t} \nabla V\left[\mathbf{r}_g^{\text{SFA}}(s) + \boldsymbol{\Sigma}(s)/\omega^2\right] ds. \tag{9b}$$

The CCSFA is also used in a semiclassical framework in Refs. [32,34–36] and in a classical framework in Refs. [17,18,37–40]. As mentioned above, the CCSFA is valid to determine the correction of the Coulomb interaction for short times (e.g., $t - t_0 \sim T$) regardless of the ellipticity. Looking at Eq. (8a), if the initial drift momentum of the electron $\mathbf{p}_{g,0}$ is sufficiently large, the Coulomb correction (9b) is significant only for a short time after ionization. According to the PPT theory, the initial drift momentum is of order $|\mathbf{p}_{g,0}| \sim \xi E_0/\omega$, hence, we expect the CCSFA to be valid in ATI only for large ellipticity.

The integrals in Eqs. (9) are computed numerically. If the initial drift momentum of the T trajectory is large, the integrand in Eq. (9b) is large for a very short time after ionization, so we make the approximation $\mathbf{E}(t) \approx \mathbf{E}(t_0) + \omega^2(t - t_0)\mathbf{A}(t_0) - \omega^2(t - t_0)^2\mathbf{E}(t_0)/2$. As a consequence, the SFA trajectory (8a) is quadratic in time. Taking $V(\mathbf{r}) \approx -1/|\mathbf{r}|$ and the initial conditions of the T trajectory to be such that $P_\perp(t - t_0) \ll |\mathbf{r}_0| + (t - t_0)^2|\mathbf{E}(t_0)|/2$ (which becomes valid at high intensity) the correction of the asymptotic drift momentum is given by

$$\Delta\mathbf{p}_g \approx \frac{\pi\,\hat{\mathbf{n}}_\parallel(t_0)}{(2|\mathbf{r}_0|)^{3/2}\sqrt{|\mathbf{E}(t_0)|}} - \frac{P_\perp\,\hat{\mathbf{n}}_\perp(t_0)}{2|\mathbf{r}_0|^2|\mathbf{E}(t_0)|}. \tag{10}$$

In Ref. [17] a similar result is derived for $P_\perp = 0$.

4. Guiding-center model

An alternative way to include the Coulomb interaction is to consider the averaged motion of the electron [24,25]. In Refs. [24,25] we showed the electron trajectory can be viewed as oscillating around a GC trajectory with constant energy. Assuming that one laser cycle is short compared to the characteristic time of the ionized electron trajectory, the ordering parameter ϵ is such that the laser frequency is large, i.e., $\omega \mapsto \omega/\epsilon$, and the Hamiltonian may be written

$$H_g(\mathbf{r}_g, \mathbf{p}_g, t) = \epsilon\left[\frac{|\mathbf{p}_g|^2}{2} + V[\mathbf{r}_g + \epsilon^2 \boldsymbol{\Sigma}(t)/\omega^2]\right]. \tag{11}$$

Averaging Hamiltonian (11) over the fast timescale [24,25], at the second order in the ordering parameter ϵ, leads to

$$\bar{H}_g(\bar{\mathbf{r}}_g, \bar{\mathbf{p}}_g) = \frac{|\bar{\mathbf{p}}_g|^2}{2} + V(\bar{\mathbf{r}}_g). \tag{12}$$

The initial conditions of the GC trajectory are given by Eqs. (7). The reconstructed electron trajectory is given by inverting Eqs. (5), where $[\bar{\mathbf{r}}_g(t), \bar{\mathbf{p}}_g(t)]$ are the trajectories of Hamiltonian (12). Therefore, the electron oscillates around its GC motion described by Hamiltonian (12). The GC Hamiltonian is invariant under time translation, implying that the energy of the GC, denoted $\mathcal{E} = \bar{H}_g(\bar{\mathbf{r}}_g, \bar{\mathbf{p}}_g)$, is conserved. In addition, for a rotationally invariant potential as in the case of atoms and in particular the soft Coulomb potential used in this article, the angular momentum of the GC, denoted $\mathbf{L} = \bar{\mathbf{r}}_g \times \bar{\mathbf{p}}_g$, is also conserved. Hence, there are as many conserved quantities as degrees of freedom, and Hamiltonian (12) is integrable.

If $\mathcal{E} > 0$, the GC motion is unbounded and the electron reaches the detector. If $\mathcal{E} < 0$, the GC motion is bounded and the electron is captured in a Rydberg state. We note that the rescattering process which induces a jump in energy $\mathcal{E}$ (see Ref. [25]), is not included in the GC model. Hence, the GC model is well suited to describe the direct ionization and the electron motion before and after rescattering, but not during. By substituting $\tau \approx \sinh^{-1}(\gamma\sqrt{\xi^2+1})$ (which holds for all ellipticities if $\gamma \lesssim 5$, see Ref. [41]) and considering $|\mathbf{E}(t_0)| \sim E_0$ in Eq. (2), the typical distance between the electron and the ionic core after tunnel ionization is $|\mathbf{r}_0| \sim (E_0/\omega^2)(1 - \sqrt{1+\gamma^2})$. The GC model is quantitatively accurate when $|\mathbf{r}_0| \gtrsim E_0/\omega^2$ [25], and as a consequence, we expect the GC model to be quantitatively accurate for $\gamma \gtrsim 1.6$.

III. PHOTOELECTRON MOMENTUM DISTRIBUTIONS (PMDs)

The laser-atom interaction gives rise to complex phenomena, involving multiple temporal and spatial scales. The phenomena arising from short timescale and long timescale processes manifest themselves in different aspects of the measurements, for different values of the parameters, and also at distinct times along the same trajectory. The multiple temporal and spatial scales arise from the competition between the strong laser and Coulomb forces. The rescattering of the electron or the subcycle recollisions occur close to the core over a short time compared to the laser cycle, and as a consequence, these processes involve short temporal and spatial scales. In contrast, Rydberg state creation and Coulomb-driven recollisions involve a contribution of the Coulomb potential on long temporal and spatial scales.

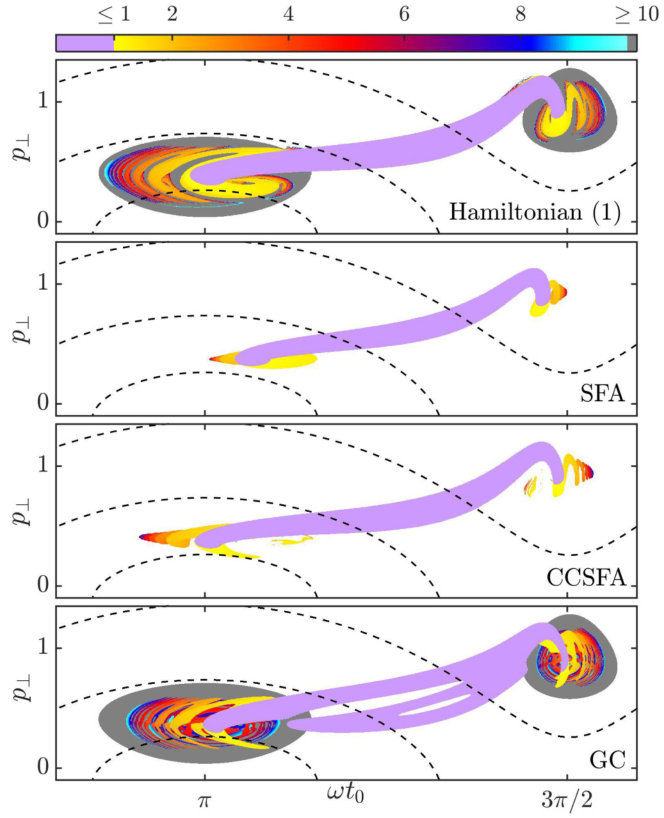

FIG. 1. Excursion time of the electron Δt per laser cycle T as a function of the initial conditions $(t_0, p_\perp, p_\parallel = p_{z,0} = 0)$ for $I = 8 \times 10^{13}$ W cm^{-2} and $\xi = 0.4$ of the reference Hamiltonian (1), the SFA [1], the CCSFA [17], and the GC [24] models. The time Δt is the smallest positive time such that $|\mathbf{r}(t_0 + \Delta t)| = 5$ a.u. The gray regions are where the electron final energy is negative after the end of the pulse (at $t = 10T$). The white regions are where the electron undergoes a direct ionization, i.e., an ionization without returning to the core. The black dashed lines are contours of constant ionization rate $W(t_0, p_\perp \hat{\mathbf{n}}_\perp(t_0))$ (see Appendix A) for $W/\max(W) = 10^{-1}$, 10^{-5}, and 10^{-15}, from bottom to top. The momentum $p_\perp$ is scaled by E_0/ω.

The coexistence of short vs long timescale processes is illustrated in Fig. 1, which shows the excursion time per laser cycle $\Delta t/T$ of the electron before it returns to the core for the reference Hamiltonian (1), the SFA, the CCSFA, and the GC models. The excursion time Δt is the smallest positive time such that $|\mathbf{r}(t_0 + \Delta t)| = R$, with $R = 5$ a.u. (we have checked that the patterns observed in Fig. 1 are robust with respect to the threshold R). For Hamiltonian (1), we observe four main features of the electron dynamics: The electron ionizes directly after ionization without return to the core (white region), the electron is trapped in a Rydberg state (gray regions), the electron returns to the core on a subcycle timescale (light purple region for which $\Delta t/T \leqslant 1$), and the electron returns to the core after multiple laser cycles (colored layers in the gray regions for which $\Delta t/T > 1$).

We observe that the region with subcycle recollisions (for which $\Delta t/T \leqslant 1$) is well described by the SFA and the CCSFA. In these regions, hard recollisions [39] and soft recollisions [37] coexist, depending on the initial conditions. However, the long timescale processes are not captured by the SFA and the CCSFA. On the other hand, the short timescale processes, which occur close to the core, are not well captured by the GC model. As we shall see in Sec. IV, what is well captured by the GC model is long timescale processes such as Rydberg state creation (gray regions) and Coulomb-driven recollisions (for which $\Delta t/T > 1$). Figure 1 reflects the complementarity of the CCSFA and the GC models on short vs long timescale processes. For shorter plateau duration, the number of layers attributed to the Coulomb-driven recollisions is reduced (not shown here). The reason is investigated in Sec. IV A. According to the PPT ionization rate, these long timescale processes are the most probable as seen in Fig. 1, and these processes are not well captured by the SFA and CCSFA models.

In this section we analyze the influence of short vs long timescale microscopic phenomena on macroscopic measurements like the photoelectron momentum distributions in light of the reduced models described in the previous section, in particular the CCSFA and the GC models, and their complementarity.

A. Short timescale dynamics

First, we consider a circularly polarized (CP) field ($\xi = 1$), used for attoclock measurements [42,43]. For ellipticity close to 1, the initial drift momentum is large and the electron moves away from the ionic core quickly. Therefore, the corrections due to the Coulomb potential on the electron trajectories occurs on a short timescale, and we expect the CCSFA to be accurate. In attoclock measurements, the observable is the offset angle Θ. We assume that it corresponds to the scattering angle of the T-trajectory

$$\Theta = \tan^{-1}(P_y/P_x),$$

where $\mathbf{P} = P_x\hat{\mathbf{x}} + P_y\hat{\mathbf{y}}$ is the T-trajectory final momentum. In order to see the Coulomb asymmetry in a PMD from a CP field, a short laser pulse has to be used [42,43]. Otherwise, the PMD would resemble a ring around the origin. Figure 2 shows the T-trajectory final momentum as a function of the intensity I for $\xi = 1$. For P_y (upper panel) we notice that the dashed black curves (CCSFA), the solid black curves (GC model), and the crosses [reference Hamiltonian (1)] overlap for $I \in [10^{12}, 10^{16}]$ W cm^{-2}, and hence a good agreement between these three models is observed. In addition, we notice that the value of P_y predicted by these three models is lower compared to the SFA model. This is a microscopic (at the level of the trajectory) signature of the Coulomb focusing. Concerning the green (light gray) dashed curve [which is the approximation of the CCSFA given by Eqs. (10)], we observe that the approximation of the CCSFA [Eqs. (9)] becomes good only at high intensity $I \gtrsim 10^{15}$ W cm^{-2}, where the drift momentum $|\mathbf{p}_{g,0}| \sim E_0/\omega$ is very large and where the electron spends a very short time close to the ionic core. At a very high intensity $I \sim 10^{16}$ W cm^{-2}, all models converge to the same value predicted by the SFA $P_y^{\mathrm{SFA}} = (E_0/\omega)/\sqrt{2}$.

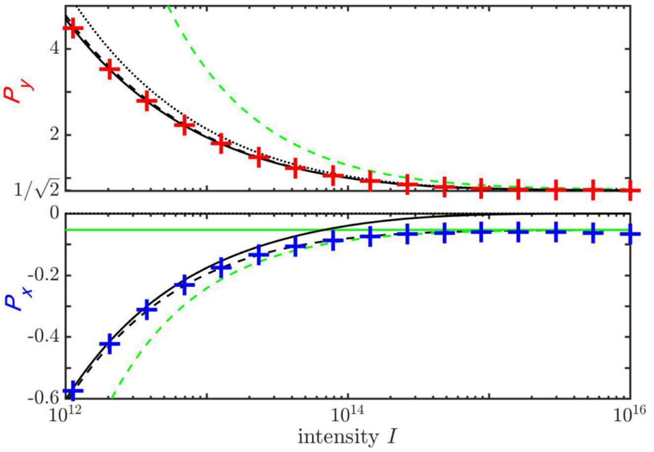

FIG. 2. T-trajectory final momentum $\mathbf{P} = P_x\hat{\mathbf{x}} + P_y\hat{\mathbf{y}}$ as a function of the laser intensity I for $\xi = 1$. The crosses are the T-trajectory final momentum of the reference Hamiltonian (1), where P_x and P_y are in blue (lower panel) and red (upper panel), respectively. The dotted, dashed, and solid black curves are the T-trajectory final momentum of the SFA, the CCSFA, and the GC model, respectively. The dashed and solid green (light gray) lines are the approximated and the asymptotic T-trajectory final momentum using Eqs. (10) and (13), respectively. The momenta are scaled by E_0/ω and the intensity is in W cm^{-2}.

For P_x (lower panel) we observe that the dashed black curves (CCSFA) and the crosses [Hamiltonian (1)] overlap for $I \in [10^{12}, 10^{16}]$ W cm^{-2}. The solid black curve (GC model) agrees well with the crosses [reference Hamiltonian (1)] only for intensities such that $I \lesssim 8 \times 10^{13}$ W cm^{-2}. This intensity range corresponds to a Keldysh parameter $\gamma \gtrsim 1.6$ for which the electron initial position is $|\mathbf{r}_0| \gtrsim E_0/\omega^2$, i.e., for which the GC model is quantitatively accurate. When the electron ionizes close to the ionic core, there is a large contribution of the Coulomb potential. Mapping the electron coordinates to its GC coordinates [Eq. (5)], and evaluating the Coulomb interaction on its GC only [Hamiltonian (12)] leads to a significant underestimate of the Coulomb effect if the electron is initially close to the ionic core. In the CCSFA, the evaluation of the Coulomb potential is performed on the approximate solution of the SFA. As a consequence, on a short timescale after ionization, the evaluation of the Coulomb interaction is performed on a position which is close to the real trajectory [Hamiltonian (1)] and therefore close to the core.

We also observe that the dotted curve (SFA, $P_x^{\mathrm{SFA}} = 0$) never agrees with the crosses [reference Hamiltonian (1)], even at very high intensity. This is a microscopic signature of the Coulomb asymmetry. In particular, we observe that the Coulomb asymmetry persists even for high intensity. For $I \gtrsim 10^{15}$ W cm^{-2}, we observe that the dashed green (light gray) curve [Eq. (10)] agrees well with the dashed black curve (CCSFA) and the crosses [reference Hamiltonian (1)]. For very high intensities, or equivalently for a very small Keldysh parameter, the correction to the T-trajectory final momentum using Eq. (10) becomes

$$\lim_{E_0\to\infty} \frac{\Delta\mathbf{p}_g}{(E_0/\omega)} = -\frac{\omega\pi\ \hat{\mathbf{x}}}{(2I_p)^{3/2}\sqrt{\xi^2+1}}, \tag{13}$$

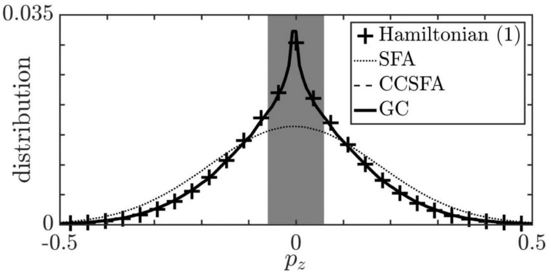

FIG. 3. Projection of the photoelectron momentum distributions (PMDs) along p_z for $I = 8 \times 10^{13}$ W cm^{-2} and $\xi = 0.4$ of the reference Hamiltonian (1), the SFA [1,13], the CCSFA [17], and the GC model. The CCSFA and the GC curves overlap. The shaded region corresponds to $|p_z| < 0.05$ a.u. The momentum p_z is scaled by E_0/ω.

which is valid for high ellipticity. The offset angle measured in an attoclock experiment is for high intensity

$$\lim_{E_0\to\infty} \Theta = \pi - \tan^{-1} \frac{\xi (2I_p)^{3/2}}{\omega\pi}.$$

The larger the intensity, the closer to the core the electron is initiated, and thus the T trajectory remains deflected by the ionic core. In addition, in the reference Hamiltonian (1), the larger the intensity, the larger the laser-atom interaction $\mathbf{r} \cdot \mathbf{E}(t)$ and the Coulomb potential contribution $V(\mathbf{r})$ at the tunnel exit. Therefore, the competition between the Coulomb potential and laser interaction is always present even at high intensity, as shown in Ref. [26]. Consequently, the Coulomb asymmetry persists even at very high intensity. Notice that these results do not depend on the shape of the laser pulse, and are still true for ultrashort pulses.

In summary, as expected for large ellipticities (i.e., close to CP), there is a very good agreement between the CCSFA [Eqs. (9)] and the reference model [Hamiltonian (1)] for all intensities. Indeed, for large ellipticities, the electron initial drift momentum is also large, and the Coulomb potential acts significantly on the electron trajectory for a short time after ionization. The Coulomb interaction causes the deflection of the T trajectory after ionization. For intensities $I \gtrsim 8 \times 10^{13}$ W cm^{-2}, the GC model also captures this effect well.

B. Long timescale dynamics

For lower ellipticities, we show that important properties of the system arising from long timescale processes, in particular Coulomb-driven recollisions and Rydberg state creation, are well described by the GC model. To illustrate this, we consider an intensity $I = 8 \times 10^{13}$ W cm^{-2} ($\gamma \sim 1.6$) and an ellipticity $\xi = 0.4$.

1. Analysis of the ionized electron momentum

Figure 3 shows the projection of the photoelectron momentum distribution on the perpendicular momentum p_z. For the reference Hamiltonian (1), the distribution presents a cusplike peak at zero perpendicular momentum. In Ref. [44] a similar shape of the distribution along the perpendicular momentum measured in experiments and with CTMC calculations has been reported. In the SFA, the drift momentum is conserved, and therefore the distribution does not change with time. As a result, the asymptotic distribution is Gaussian, in contrast with the results with the reference Hamiltonian (1) and in experiments [44]. The distribution of the CCSFA and the GC models overlap. In agreement with the observations of Ref. [44], this cusp is due to the long-range Coulomb interaction between the ionized electron and the core

Next, we focus on the part of the PMDs for which $|p_z| < 0.05$ a.u. (shaded region in Fig. 3). Figure 4 shows the PMDs computed with CTMC simulations of the reference Hamiltonian (1), the SFA [Eqs. (8)] [1,13], the CCSFA [Eqs. (9)] [17], and the GC model [Hamiltonian (12)]. The T-trajectory final momentum is shown with a black dot for each model. The PMDs are mainly composed of two clouds centered around the T-trajectory final momentum. The two clouds are roughly symmetric with respect to the origin according to the symmetry $(\mathbf{r}, \mathbf{p}, t) \mapsto (-\mathbf{r}, -\mathbf{p}, t + T/2)$ of the reference Hamiltonian (1) for a constant laser envelope ($f = 1$) which is also preserved by the initial conditions [see Eq. (2)] and the reduced models.

For the reference Hamiltonian (1), the PMD in the leftmost panel of Fig. 4 exhibits three significant features: The asymmetry with respect to the $\hat{\mathbf{y}}$ axis, the relatively high density of electrons with near-zero momentum—corresponding to near-zero-energy photoelectrons [45]—and the tails for high momentum (regions for $|p_x| > 1$). In order to interpret these features, we compare this PMD with those of the three reduced models. The CTMC approach we use does not take into account any effects due to the absorption of photons or interference after ionization, which lead for example to the rings in ATI [46]. These would of course be included in a time-dependent Schrödinger equation (TDSE) calculation, but also in other kinds of semiclassical calculations.

In the PMD of the SFA [1,13] (second panel of Fig. 4 from the left), the two clouds are symmetric with respect to the $\hat{\mathbf{y}}$ axis, there is a lack of near-zero-energy photoelectrons, and there are no tails for high momentum. Therefore, these effects observed in the PMD of Hamiltonian (1) are a consequence of the Coulomb potential, which is expected to be significant here since the characteristic time of the ionized trajectories is long compared to one laser cycle.

In the PMD of the CCSFA [17] (third panel of Fig. 4 from the left), the two clouds are asymmetric with respect to the $\hat{\mathbf{y}}$ axis. As discussed in the previous section, after ionizing, the electron trajectories deviate because of the Coulomb interaction: This asymmetry is the Coulomb asymmetry. With the CCSFA, however, we observe that the distribution is very low around the origin of momentum space, i.e., there is still a lack of near-zero-energy photoelectrons. Indeed, the drift momentum of the near-zero-energy photoelectrons is low and the conditions on the validity of the CCSFA are not met. We notice that the integrals we compute numerically for determining the correction to the final momentum of the electron [Eqs. (9)] do not always converge. Obviously the integrals diverge if for instance $\mathbf{p}_{g,0} = \mathbf{0}$. Also, for small drift momentum, it is challenging to obtain numerically converged integrals. Finally, we observe tails for $|p_x| > 1$ in the PMD of the CCSFA like in the PMD of Hamiltonian (1).

In the PMD of the GC model (rightmost panel of Fig. 4), the clouds are asymmetric with respect to the $\hat{\mathbf{y}}$ axis. After

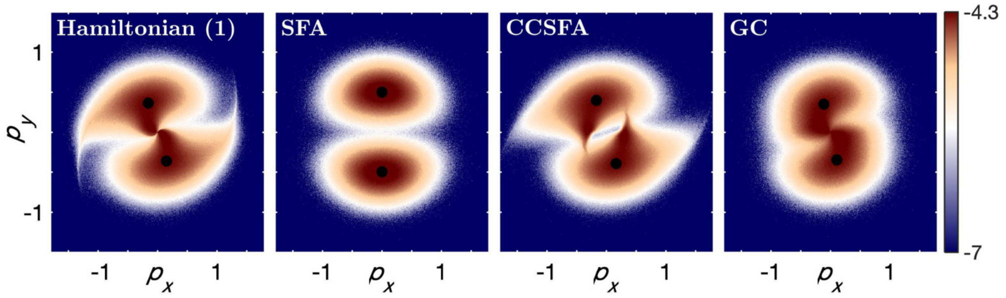

FIG. 4. Photoelectron momentum distributions (PMDs) for $|p_z| < 0.05$ in logarithmic scale for $I = 8 \times 10^{13}$ W cm^{-2} and $\xi = 0.4$ of the reference Hamiltonian (1), the SFA [1,13], the CCSFA [17], and the GC model. The upper (lower) black dot is the T-trajectory final momentum for each model (its symmetric momentum with respect to the origin). The momenta are scaled by E_0/ω.

ionizing, the electron trajectories are deflected by the Coulomb force exerted on their GC [24]. One advantage of this model is that the final momentum of the electron has an explicit expression for $V(\bar{\mathbf{r}}_g) \approx -1/|\bar{\mathbf{r}}_g|$ (see Appendix B), and as a consequence the computations of the CTMCs are as fast as the computation of the CTMCs of the SFA. Moreover, this model does not rely on computing integrals that may or may not converge. In addition, we observe that the asymmetric clouds are connected to the origin of the momentum space, showing that the near-zero-energy photoelectrons which ionize directly are well captured by this model. We distinguish the near-zero-energy photoelectrons which ionize directly from the near-zero-energy electrons induced by rescattering; the latter are the cause of the low-energy structure (LES) [39,47] in the photoelectron energy spectra. However, the absence of tails in the GC model suggests that the tails observed in the reference model and the CCSFA are the contribution of rescattered electrons [37,48].

Hence, the asymmetry observed in the PMD of the reference Hamiltonian (1) is also captured by the reduced models of the CCSFA and the GC. This asymmetry is due to the deviation of the electrons or their GC originating from the Coulomb interaction. In addition, near-zero-energy photoelectrons are captured by the GC model. The tails in the PMDs are due to the rescattering of electrons that have experienced a recollision [37], in which the electron comes close to the ionic core and is rescattered due to the competitive forces between the laser and the Coulomb interaction. This short timescale process is well known and well described by the CCSFA (see, e.g., Refs. [37,39,40,48]).

2. Analysis of the initial conditions

We investigate the initial conditions of the electron after tunnel ionization to interpret and understand the origin of the near-zero-energy photoelectrons. Figure 5 shows the final energy of the electron as a function of its initial conditions after tunneling for $I = 8 \times 10^{13}$ W cm^{-2} and $\xi = 0.4$ for the reference Hamiltonian (1), the SFA [Eqs. (8)] [1,13], the CCSFA [Eqs. (9)] [17], and the GC model [Hamiltonian (12)]. The space of initial conditions is restricted to $p_\parallel = p_{z,0} = 0$, which is the most probable initial longitudinal and perpendicular momentum.

For the reference Hamiltonian (1) (upper panel of Fig. 5), we observe two gray regions of initial conditions where the electron final energy is negative, i.e., in which the electron is trapped in Rydberg states [28]. The color corresponds to the final energy of photoelectrons which have reached

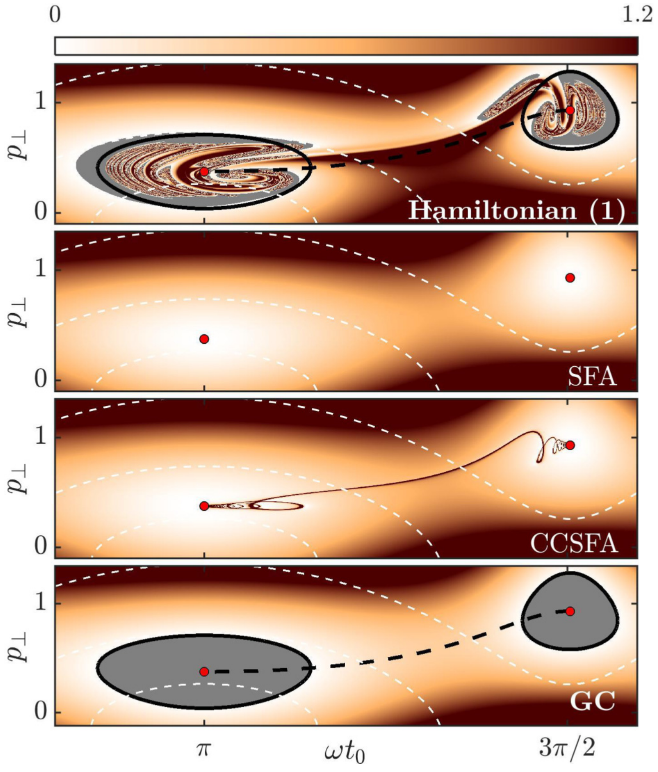

FIG. 5. Electron final energy as a function of the initial conditions $(t_0, p_\perp, p_\parallel = p_{z,0} = 0)$ for $I = 8 \times 10^{13}$ W cm^{-2} and $\xi = 0.4$ of the reference Hamiltonian (1), the SFA [1,13], the CCSFA [17], and the GC model (12). In gray-colored regions, the electron final energy is negative. The white dashed lines are contours of constant ionization rate $W(t_0, p_\perp \hat{\mathbf{n}}_\perp(t_0))$ (see Appendix A) for $W/\max(W) = 10^{-1}$, 10^{-5}, and 10^{-15}, from bottom to top. The red dots correspond to the initial conditions for which the electron final energy in the SFA is zero, i.e., $\mathcal{E}^{\mathrm{SFA}} = 0$ [see Eq. (14)]. The solid black lines correspond to the initial conditions for which the GC energy is zero, i.e., $\mathcal{E} = 0$ [see Eq. (15)]. The black dashed line corresponds to the initial conditions for which the GC angular momentum is zero and the initial radial momentum is negative, i.e., $\mathbf{L} = \mathbf{0}$ and $p_r(t_0) < 0$, where $\mathbf{L} = \bar{\mathbf{r}}_g \times \bar{\mathbf{p}}_g$ and $p_r = \bar{\mathbf{p}}_g \cdot \bar{\mathbf{r}}_g/|\bar{\mathbf{r}}_g|$. The momentum and the energy are scaled by E_0/ω and $\mathrm{U}_p = E_0^2/4\omega^2$, respectively.

the detector. Enclosed by the gray regions, we observe that there are ionized electrons whose energy depends extremely sensitively on the initial conditions, as a signature of the rescattering process (see also the uppermost panel of Fig. 1). The boundaries of the gray regions are surrounded by regions of near-zero-energy photoelectrons which ionize directly. The part of the gray region with small $p_\perp$ (lower part of the left gray regions) is in a region where the ionization rate is high. As a consequence, a significant number of electrons which ionize directly reach the detector with near-zero energy, as observed in the leftmost panel of Fig. 4.

For the SFA [1,13], the final momentum of the electron is given by its initial drift momentum $\mathbf{p}_{g,0}$ since it is constant in time. As a consequence, the electron final energy is

$$\mathcal{E}^{\mathrm{SFA}} = \frac{|\mathbf{p}_{g,0}|^2}{2}. \qquad (14)$$

In the SFA (second panel from the top of Fig. 5), only two initial conditions lead to near-zero-energy electrons, located at $p_\perp = -(E_0/\omega)\xi/\sqrt{\xi^2+1}$ and $\omega t_0 = \pi$, and at $p_\perp = -(E_0/\omega)/\sqrt{\xi^2+1}$ and $\omega t_0 = 3\pi/2$, represented by red dots in Fig 5. These initial conditions are located where the ionization rate is one or several orders of magnitude lower than the maximum ionization rate. The consequence is a lack of near-zero-energy photoelectrons in the PMD for the SFA observed in Fig. 4.

For the CCSFA [17] (third panel from the top of Fig. 5), we observe the same patterns as for the SFA. The initial conditions of the near-zero-energy photoelectrons which ionize directly for the CCSFA are located in the same region of low ionization rate as for the SFA. Here again, the consequence is the lack of near-zero-energy electrons for the CCSFA observed in Fig. 4. However, we observe in the CCSFA a region with an abrupt change of energy with initial conditions across the dark colored path connecting the two red dots, absent in the SFA. This path is also present in the reference Hamiltonian (1). It is due to the rescattering process, i.e., the correction of the momentum of the CCSFA due to a recollision in the SFA (see second panel from the top of Fig. 1). Furthermore, this path separates near-zero-energy photoelectrons induced by rescattering—responsible for the LES in the photoelectron energy spectra [39,47]—from high energy photoelectrons. The CCSFA has been used to describe these short timescale processes (see for instance Refs. [37,39,40,48]).

The final energy of the electron using the GC model is given by

$$\mathcal{E} = \frac{|\mathbf{p}_{g,0}|^2}{2} + V(\mathbf{r}_{g,0}). \qquad (15)$$

The GC energy allows us to clearly distinguish two types of trajectories: Trajectories with $\mathcal{E} > 0$ and $\mathcal{E} < 0$. The set of initial conditions for which $\mathcal{E} < 0$ is referred to as the rescattering domain. Comparing the lowest panels of Figs. 1 and 5, this definition of the rescattering domain includes the Rydberg state creations, the Coulomb-driven recollisions, and the subcycle recollisions most weighted by the PPT ionization rate. Notice that this definition misses a piece of the light purple band between the two rescattering domains in Fig. 1, which carries a lower weight according to the PPT ionization rate for all ellipticities. In the top panel of Fig. 5 we observe that the condition $\mathcal{E} < 0$ determines well the gray region of initial conditions in the reference Hamiltonian (1). The initial conditions for which the electron final energy is zero in the SFA are contained inside this region. The Coulomb potential creates this region in which the GC motion is bounded, which allows the electron to come back to the ionic core and to rescatter after multiple laser cycles, or to be trapped into Rydberg states, scenarios analyzed in Sec. IV. The boundaries of this rescattering domain correspond to the initial conditions for which the electron final energy is zero, i.e., $\mathcal{E} = 0$. We observe that the inclusion of the Coulomb potential pushes down the near-zero-energy photoelectrons to regions in momentum space for which the ionization rate is higher. As a consequence, we observe a significant number of near-zero-energy photoelectrons in the PMD of the GC model. Moreover, we notice that $\mathcal{E} = \mathcal{E}^{\mathrm{SFA}} + V(\mathbf{r}_{g,0})$, and since the Coulomb potential is strictly negative, it is evident that electrons lose energy because of the Coulomb interaction, i.e., that electrons are subjected to Coulomb focusing.

3. Types of trajectories

In order to understand the origin of the sensitivity to initial conditions observed in the rescattering domain, we analyze the different types of trajectories. Figure 6(a) shows the scattering angle of the electron, whose trajectory is obtained from the reference Hamiltonian (1), as a function of the initial conditions $(t_0, p_\perp)$ for $\xi = 0.4$. The scattering angle corresponds to the angle between momentum of the ionized electron $\mathbf{p}$ at infinity and the major polarization axis ($\hat{\mathbf{x}}$ axis). In Figs. 6(b)–6(e) the dark blue (dark gray) curves are the trajectories of the electron of Hamiltonian (1), with initial conditions indicated by the corresponding markers in Fig. 6(a). The cyan (light blue) curves are the GC trajectories of Hamiltonian (12). For Figs. 6(c)–6(e) [as well for Figs. 7(d), 7(e) and 9(d)], the GC is initialized far from the ionic core (for $|\mathbf{r}| \gtrsim 2E_0/\omega^2$), during the plateau, in the domain of validity of the GC model (see Sec. V B 4 for a study of the discrepancy between the GC and the electron trajectory).

Figure 6(b) shows a subcycle recollision. The initial condition of this trajectory is near the condition for which the GC angular momentum is $\mathbf{L} = \bar{\mathbf{r}}_g \times \bar{\mathbf{p}}_g \approx \mathbf{0}$ and the initial GC radial momentum is negative, and corresponds to the light purple region in the uppermost panel of Fig. 1. Right after ionization, the GC trajectory is (mostly) straight, brings the electron to the core, and the electron recollides. The recollision occurs in a timescale shorter than one laser cycle, referred to as a subcycle recollision. We notice that if the electron tunnel ionizes further away from the ionic core, the same conditions (near zero GC angular momentum and negative initial radial momentum) could lead to a multiple laser-cycle recollision. Looking at the third panel from the top of Fig. 1, we observe that this type of recollisions, for which $\mathbf{r}_{g,0} \cdot \mathbf{p}_{g,0} < \mathbf{0}$ and $\mathbf{r}_{g,0} \times \mathbf{p}_{g,0} \approx \mathbf{0}$, are well predicted by the CCSFA.

Figure 6(c) shows a direct ionization. The initial condition of this trajectory is in a regular region, for which the GC energy is positive $\mathcal{E} > 0$. The GC trajectory is unbounded, and leaves the ionic core region. The electron also leaves the ionic core region, driven by its GC.

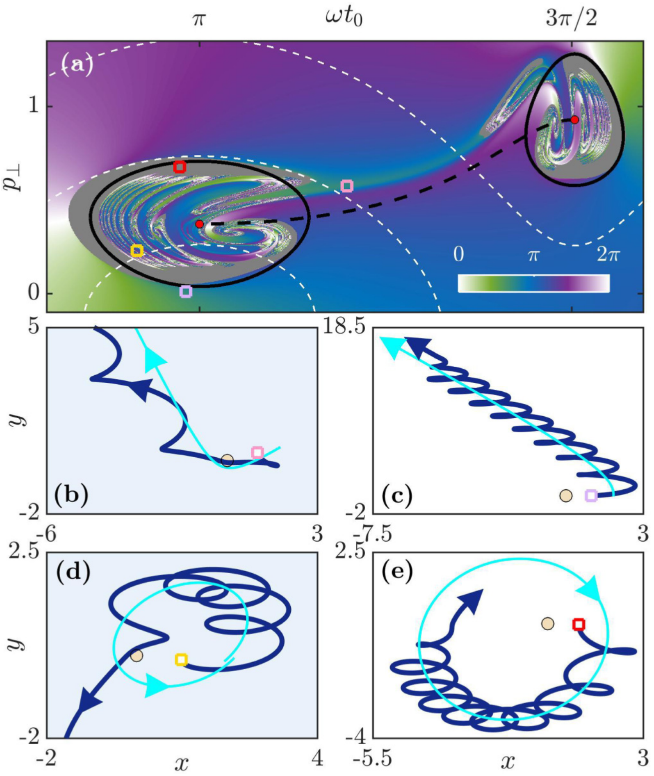

FIG. 6. (a) Scattering angle of the electron as a function of the initial conditions after tunneling (t_0, $p_\perp$, $p_\parallel = p_{z,0} = 0$) for $I = 8 \times 10^{13}$ W cm^{-2} and $\xi = 0.4$. The white dashed lines are the contours of constant ionization rate $W(t_0, p_\perp \hat{\mathbf{n}}_\perp(t_0))$ (see Appendix A) for $W/\max(W) = 10^{-1}$, 10^{-5}, and 10^{-15}, from bottom to top. The red dots correspond to the initial conditions for which $\mathcal{E}^{\rm SFA} = 0$ [see Eq. (14)]. The solid black line corresponds to the initial conditions for which $\mathcal{E} = 0$ [boundaries of the rescattering domain for the GC model, see Eq. (15)]. The black dashed line corresponds to the initial conditions for which the GC angular momentum is zero and the initial radial momentum is negative, i.e., $\mathbf{L} = \mathbf{0}$ and $p_r(t_0) < 0$, where $\mathbf{L} = \bar{\mathbf{r}}_g \times \bar{\mathbf{p}}_g$ and $p_r = \bar{\mathbf{p}}_g \cdot \bar{\mathbf{r}}_g / |\bar{\mathbf{r}}_g|$. Gray areas show the conditions for which the electron is trapped into Rydberg states. (b)–(e) Dark blue (dark gray) and cyan (light gray) curves are the electron and its GC trajectory, respectively. The initial condition of each trajectory is associated with a marker represented in (a). These trajectories represent a typical: (b) subcycle recollision, (c) direct ionization, (d) Coulomb-driven recollision, and (e) Rydberg state creation. Panels (b) and (c) have positive GC energy, while (d) and (e) have negative GC energy. Shaded panels indicate the cases with recollisions. The momentum and position are scaled by E_0/ω and E_0/ω^2, respectively.

Figure 6(d) shows a Coulomb-driven recollision. The initial condition of this trajectory is in one of the main chaotic regions, for which the GC energy is negative $\mathcal{E} < 0$, corresponding to the colored layers in the uppermost panel of Fig. 1. The GC trajectory is bounded. As a consequence, the electron returns to the ionic core, driven by its GC, and recollides with the ionic core. After rescattering, the GC energy jumps to another energy level [25], and the electron could ionize.

Figure 6(e) shows a Rydberg state creation. The initial condition of this trajectory is in the gray area, for which the GC energy is negative $\mathcal{E} < 0$. The GC trajectory is bounded. However, contrary to the Coulomb-driven recollision [Fig. 6(d)], the laser pulse ends before the occurrence of the recollision. The Rydberg state creation corresponds to a frustrated Coulomb-driven recollision. The laser pulse duration plays an important role in determining the ratio between Coulomb-driven recollisions and Rydberg state trapping (see Sec. IV A).

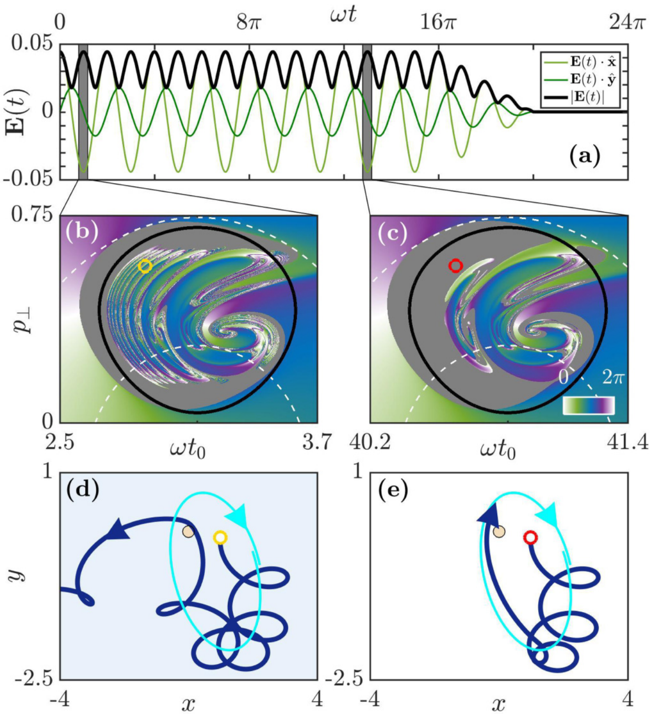

FIG. 7. (a) Electric field components and amplitude as a function of ωt. The gray regions indicate the ionization time for which the final scattering angle is computed in (b) and (c). (b) and (c) Final scattering angle of the ionized electron as a function of the initial conditions (ωt_0, $p_\perp$, $p_\parallel = p_{z,0} = 0$) for $I = 8 \times 10^{13}$ W cm^{-2} and $\xi = 0.4$ for the reference Hamiltonian (1). The white dashed lines are the contour plot of the ionization rate $W(t_0, p_\perp \hat{\mathbf{n}}_\perp(t_0))$ (see Appendix A) for $W/\max(W) = 10^{-1}$, 10^{-5}, and 10^{-15}, from bottom to top. The solid black line corresponds to the initial conditions for which $\mathcal{E} = 0$ [boundaries of the rescattering domain for the GC model, see Eq. (15)]. The dark gray region corresponds to the initial conditions for which the electron is trapped into a Rydberg state at the end of the pulse. (d) and (e) Dark blue (dark gray) and cyan (light gray) curves are the electron and its GC trajectory, respectively. The initial conditions of the trajectories in (d) and (e) are indicated by circles in (b) and (c), respectively. The trajectories in (d) and (e) are initialized at the same laser phase, but (d) is a Coulomb-driven recollision and (e) is a Rydberg state creation. The laser amplitude is in a.u., the momentum and the position are scaled by E_0/ω and E_0/ω^2, respectively.

We observe that, in the four types of trajectories, two of them cannot be predicted by the SFA. While direct ionization and one-laser-cycle rescattering [Figs. 6(c) and 6(b), respectively] are, at least qualitatively, predictable by the SFA, Coulomb-driven recollisions and Rydberg state creation [Figs. 6(d) and 6(e), respectively] are predictable only when the Coulomb potential is taken into account. In the next section we analyze Coulomb-driven recollisions and Rydberg state creation in more detail.

IV. COULOMB-DRIVEN RECOLLISIONS AND RYDBERG STATE CREATION

A. Ionization time dependence

Figures 7(b) and 7(c) show the final scattering angle of the ionized electron as a function of its initial conditions $(\omega t_0, p_\perp)$, for an ionization that takes place at the beginning of the pulse and at the end of the pulse, respectively [see Fig. 7(a)]. Figures 7(d) and 7(e) show two trajectories with the same initial momentum and the same laser phase, but with two distinct ionization times (separated by six laser cycles). Since the phase is the same, the GC trajectories [cyan (light gray) curves] in Figs. 7(d) and 7(e) are the same. Since the GC energy of these trajectories is negative, the GC trajectory is bounded.

In Fig. 7(d), for which the electron ionizes at the beginning of the plateau, we observe that the electron oscillates around the bounded GC trajectory, which drives the electron back to the ionic core. After about four oscillations around the GC trajectory, the electron comes back to the ionic core. At this time, the GC energy jumps to another energy level due to the combined Coulomb and laser interaction, and the electron ionizes. This is a Coulomb-driven recollision.

In Fig. 7(e) we observe that the electron oscillates as well around the bounded GC trajectory, which drives the electron back towards the core. However, when the electron is still far from the ionic core, the electric field is turned off, and the electron is trapped into a Rydberg state. The Rydberg state in which the electron is trapped corresponds almost to the Rydberg state of its GC.

In other words, for both trajectories of Figs. 7(d) and 7(e), the electron oscillates around the same GC trajectory. The difference between these two trajectories is the remaining time $10T - t_0$ before the laser field is turned off. In Fig. 7(d) the electron has enough time to undergo a close encounter with the ionic core ($|\mathbf{r}| < E_0/\omega^2$) before the electric field is turned off, when in Fig. 7(e) the electric field turns off sooner, while the electron is still far from the ionic core ($|\mathbf{r}| > E_0/\omega^2$). The close encounter with the ionic core distinguishes the Coulomb-driven recollision from the Rydberg state creation. The scenarios of Coulomb-driven recollision and Rydberg state creation are closely related, since in both cases, the electron oscillates around a negative-energy GC.

Looking at the excursion time per laser cycle $\Delta t/T$ of the GC model depicted in the lowest panel of Figs. 1 and 8(a), we observe similar layered patterns as for the reference Hamiltonian (1) [see uppermost panel of Figs. 1, 5(a), 6(a), 7(b), and 7(c)]. These layered patterns correspond to trajectories which spend multiple laser cycles far from the origin before returning to the ionic core, such as the one depicted in Fig. 6(d) (Coulomb-driven recollision). Each layer is associated with a range of $\Delta t/T$ around an integer number, where, for decreasing ionization time for $\omega t_0 < \pi$, $\Delta t/T$ associated with each layer increases.

In order to picture roughly the conditions for which the Coulomb-driven recollisions occur, we first approximate the potential by a hard-Coulomb potential, i.e., $V(\bar{\mathbf{r}}_g) \approx -1/|\bar{\mathbf{r}}_g|$, reducing this GC model to a Kepler problem (see also Appendix B). Then we consider the period of the orbit per laser cycle $T_g/T = \omega/(2|\mathcal{E}|)^{3/2}$ [using $V(\bar{\mathbf{r}}_g) \approx -1/|\bar{\mathbf{r}}_g|$], where T_g is referred to as the GC orbit period in what follows. Figure 8(b) shows the period of the GC orbit per laser cycle $T_g/T = \omega/(2|\mathcal{E}|)^{3/2}$ as a function of the initial conditions in the largest rescattering domain. The gray regions correspond to the regions where the GC perihelion [see Eq. (B2)]—the closest distance between the GC orbit and the ionic core—is greater than E_0/ω^2 or where $t_0 + T_g > T_f$. Figure 8(c) shows the GC distance from the ionic core $|\bar{\mathbf{r}}_g(t)|$ as a function of time per laser cycle of a sample of initial conditions indicated with the markers in Fig. 8(b), and the distance from the ionic core $|\bar{\mathbf{r}}(t)|$ of the corresponding reconstructed trajectories. We see that the color code associated with the GC orbit period T_g agrees well with the color code associated with the excursion

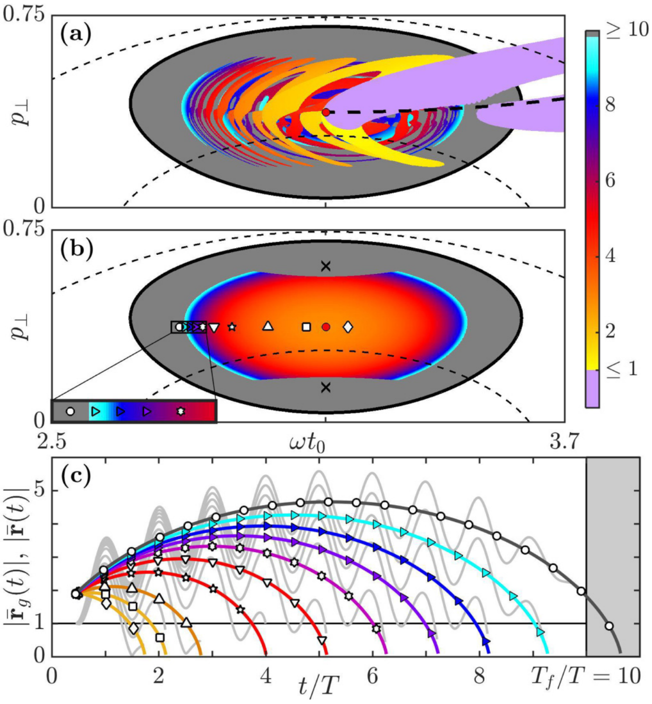

FIG. 8. Recollisions in the GC model for $I = 8 \times 10^{13}$ W cm^{-2} and $\xi = 0.4$. (a) $\Delta t/T$ as a function of the initial conditions $(t_0, p_\perp, p_\parallel = p_{z,0} = 0)$ (zoom of the lowest panel of Fig. 1 on the largest rescattering domain), where Δt is the smallest time interval such that $|\bar{\mathbf{r}}(t_0 + \Delta t)| = 5$ a.u., with $t_0 + \Delta t < T_f$ (laser pulse duration $T_f = 10T$) and $\bar{\mathbf{r}}(t) = \bar{\mathbf{r}}_g(t) + \boldsymbol{\Sigma}(t)/\omega^2$ (reconstructed trajectory). The white and dark gray regions are where this condition is never met, and where the GC energy is positive (white region) and negative (gray region). (b) $T_g/T = \omega/(2|\mathcal{E}|)^{3/2}$ (see text). The dark gray region is where the GC perihelion [see Eq. (B2)] is greater than the quiver radius $E_0/\omega^2 \approx 14$ a.u., or where $t_0 + T_g \geqslant T_f$. The inset is a zoom. The crosses are the location of the GC circular orbits (see Sec. IV B). (a) and (b) The red dots and the black thick dashed curves are the same as in Fig. 5(a). The dark dashed lines are contours of constant ionization rate $W(t_0, p_\perp \hat{\mathbf{n}}_\perp(t_0))$ (see Appendix A) for $W/\max(W) = 10^{-1}$, 10^{-5}, and 10^{-15}, from bottom to top. (c) The lines with markers are the GC trajectories $|\bar{\mathbf{r}}_g(t)|$ with initial conditions plotted in (b) with the corresponding marker and color, and the light gray lines are the reconstructed trajectories $|\bar{\mathbf{r}}(t)|$. The light gray region is when the laser field is turned off. The momenta and the positions are scaled by E_0/ω and E_0/ω^2, respectively.

time Δt in Fig. 8(a). Indeed, in Fig. 8(c) we observe that the larger the period of the GC orbit followed by the electron, the larger its excursion time. As a consequence, the GC orbit period T_g is a good observable to estimate the excursion time of the electron Δt. In addition, the GC orbit period of the trajectory associated with the leftmost marker in Fig. 8(b) is such that $t_0 + T_g > T_f$. The electron does not undergo recollision and ends up trapped in a Rydberg state since it comes back to the ionic core after the end of the laser pulse. Therefore, electrons undergoing Coulomb-driven recollisions are typically driven by GC orbits such that $T_g < T_f - t_0$.

In summary, the electron is likely to undergo a Coulomb-driven recollision if it oscillates around a GC with a negative energy $\mathcal{E} < 0$, a positive initial GC radial momentum $p_r(t_0) = \mathbf{p}_{g,0} \cdot \mathbf{r}_{g,0}/|\mathbf{r}_{g,0}| > 0$, a GC orbital period such that $T_g = 2\pi/(2|\mathcal{E}|)^{3/2} < T_f - t_0$, and a GC perihelion smaller than the quiver radius. Notice that the condition that the perihelion of the GC orbit is smaller than the quiver radius is similar to $\mathbf{L} \approx \mathbf{0}$. As a consequence, all recollisions are likely driven by small absolute values of the GC angular momentum. In contrast, the electron is likely to be trapped in a Rydberg state if it oscillates around a GC with a negative energy $\mathcal{E} < 0$ and either an orbital period greater than the laser pulse duration $T_g > T_f - t_0$ or a perihelion greater than the quiver radius, i.e., a large GC angular momentum. In the next section we show that this latter process is robust due to the existence of center-saddle periodic orbits which are weakly unstable.

B. Long plateau durations

In the lowest panel of Figs. 1 and 8(a) we notice some gray regions in the upper and lower part of the rescattering domain for which the GC orbit period is such that $T_g < T_f - t_0$. However, in these regions, the electron does not recollide because the GC perihelion is large (greater than $E_0/\omega^2 \approx 14$ a.u.), as it is shown in Fig. 9(a). As a consequence, there exists no time Δt such that $|\bar{\mathbf{r}}(t_0 + \Delta t)|$ is small, i.e., it is unlikely the electron recollides. This is also a scenario we observe in the reference model (1), in which the electron spins around the core for multiple laser cycles without recolliding.

For long plateau durations ($T_p = 100T, T_f = T_p + 2T$) and an ionization time at the beginning of the laser pulse ($t_0 \ll T_p$), we expect that electrons oscillating around a negative near-zero-energy GC (for which the GC orbit period is such that $T_g > T_f - t_0$) and electrons with a large GC perihelion [see Eq. (B2)] (GC perihelion greater than E_0/ω^2 that prevents the electron from rescattering) create Rydberg states. In Fig. 9(b) we observe indeed a pink thin layer of electrons creating Rydberg states, with a near-zero-energy GC such as the dark blue (dark gray) trajectory depicted in Fig. 9(d). In addition, we observe two regions of initial conditions with smaller values of final energy for which the electrons are trapped in Rydberg states after having remained in the vicinity of the ionic core, for which the GC perihelion is larger than the quiver radius, as shown for the dark blue (dark gray) trajectory of the reference Hamiltonian in Fig. 9(e). However, by comparing Figs. 9(a) and 9(b), we observe that not all the electrons with a GC perihelion larger than the quiver radius are captured into Rydberg states. Here we show how some electrons remain trapped while others do not.

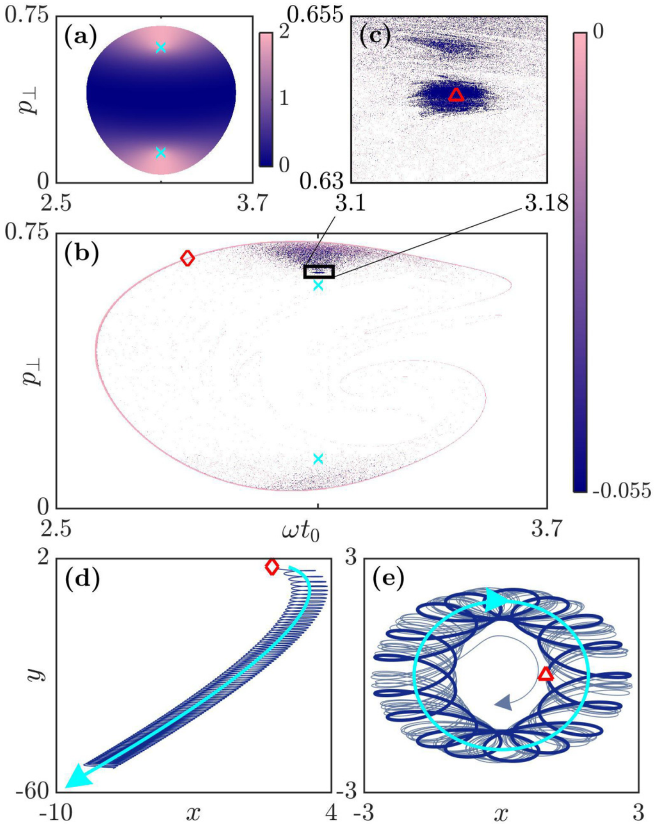

FIG. 9. The parameters are $I = 8 \times 10^{13}$ W cm^{-2}, $\xi = 0.4$ and plateau duration $T_p = 100T$. (a) GC perihelion [see Eq. (B2)] in the rescattering domain depicted in the space of initial conditions $(t_0, p_\perp, p_\parallel = p_{z,0} = 0)$. (b) Final negative energies of the electron trajectories of the reference Hamiltonian (1), where (c) is a zoom around the trapping region. The white color in (a)–(c) denotes an electron not trapped at the end of the laser pulse. (d) and (e) Trajectories for the initial conditions indicated with a diamond in (c) and a triangle in (b), respectively. The dark blue (dark gray) and cyan (light gray) curves are the electron trajectory of the reference Hamiltonian (1) and the GC trajectory, respectively. The thick dark blue (dark gray) curve in (e) is a center-saddle periodic orbit very close to the region depicted in (c). The cyan crosses in (a) and (b) are the initial conditions of the clockwise (upper cross) and anticlockwise (lower cross) circular GC orbits. The cyan (light gray) curve in (e) is the GC clockwise circular orbit, whose initial conditions are very close to the trapping region depicted in (c). The momenta and positions are scaled by E_0/ω and E_0/ω^2, respectively.

As observed in Fig. 9(c), the filled region of initial conditions leading to electrons trapped in Rydberg states with a large GC perihelion is roughly regular. Figure 9(e) shows in dark blue (dark gray) a typical trajectory of Hamiltonian (1) initiated inside this regular region. We observe that this trajectory turns around the core multiple times without being rescattered by the ionic core. As a consequence, the GC energy of this electron remains negative and roughly constant throughout the laser pulse duration [25]. When the laser field is turned off, its GC energy is still negative and the electron is trapped in a Rydberg state. Near the initial conditions of this trajectory, there is a center-saddle periodic orbit of the reference model (1) which exhibits the same pattern as this trajectory. This center-saddle periodic orbit is depicted in thick dark blue (dark gray) in Fig. 9(e). In its neighborhood, the periodic orbit is center in one plane and saddle in a transverse plane defined by the eigenvectors of the monodromy matrix associated with the complex and real eigenvalues, respectively. Hence, there are two-dimensional invariant tori surrounding the periodic orbit in the center direction. The saddle direction is weakly unstable (its eigenvalue is ~ 1.4) and the orbit period is large (period of $30T$), which implies that the unstable direction pushes slowly the electron away from each invariant torus. Consequently, trajectories in the vicinity of this periodic orbit remain close to it for relatively long times, even for long laser pulses.

In Fig. 9(a) we observe that when the GC perihelion is large (greater than E_0/ω^2), the recollisions are unlikely to happen as mentioned earlier. In these two regions of large GC perihelion, there are two cyan crosses indicating the initial conditions for which the GC orbit is circular. The initial conditions of these circular orbits are $p_\perp = \mathbf{A}(t_0) \cdot \hat{\mathbf{n}}_\perp(t_0) \pm \omega^2 / |\mathbf{E}(t_0)| \cosh \tau_0(t_0)$ with $\omega t_0 = n\pi$ and $n \in \mathbb{N}$. They are close to the regular region in Figs. 9(b) and 9(c). The circular orbit of the GC is depicted in cyan (light gray) in Fig. 9(e). We observe that the cyan (light gray) curve provides the leading behavior of the averaged trajectory of the center-saddle periodic orbit in thick dark blue (dark gray). The energy of the GC circular orbits (clockwise and anticlockwise) is given by $\mathcal{E} = -\omega^2 \sqrt{\xi^2+1}/(2E_0 \cosh \tau)$ and their perihelion by $1/(2|\mathcal{E}|)$.

In summary, there is a region of initial conditions for which the GC perihelion is larger than the quiver radius E_0/ω^2, preventing the electron to recollide with the core. Instead, the electron is trapped in a Rydberg state. We showed that this process is robust because in the neighborhood of these initial conditions, there are center-saddle periodic orbits with weakly unstable directions that keep the electron in the vicinity of the core.

C. Rate of Rydberg state creation

Next, we investigate the rate of Rydberg state creation as a function of the laser ellipticity. A Rydberg state is created if the electron energy is negative at the end of the laser pulse. In the SFA, the condition of Rydberg state creation $\mathcal{E}^{\rm SFA} = 0$ [see Eq. (14)] is a one-dimensional curve $(t_0, \mathbf{p}_0^\star(t_0))$ in a four-dimensional space $(t_0, \mathbf{p}_0)$, with $\mathbf{p}_0^\star(t_0) = \mathbf{A}(t_0)$. As a consequence, the probability of Rydberg state creation is in fact zero. In Refs. [28,49], the yield of Rydberg state creation is given by $\mathbb{Y}_{\rm SFA} = \int_0^{T_f} dt_0\, W(t_0, \mathbf{p}_0^\star(t_0))$.

Figure 10 shows the Rydberg state creation probability as a function of the laser ellipticity from CTMC simulations of the reference Hamiltonian (1) (thin solid curves with markers) and the SFA prediction (dotted curves) $\mathbb{Y}_{\rm SFA}/N$ with $N = \int_0^{T_f} dt_0 \int_{-\infty}^{\infty} d^3\mathbf{p}_0\, W(t_0, \mathbf{p}_0)$ the yield of ionized electrons. In Ref. [49] The SFA prediction is normalized such that it agrees at $\xi = 0$ with the CTMC simulations of the reference Hamiltonian (1) for $T_p = T$ (thin lines with star markers). Notice that only the prediction of the SFA is artificially normalized. For the SFA prediction (dotted curves), we observe a good agreement with the reference model at high ellipticity for all intensities and at low ellipticity for high intensity.

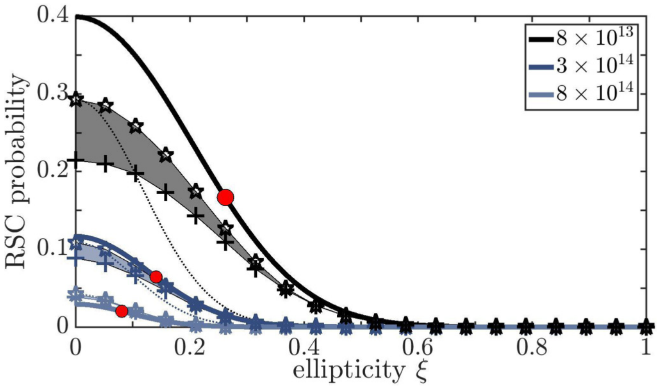

FIG. 10. Rydberg state creation (RSC) probability as a function of the laser ellipticity ξ for $I = 8 \times 10^{13}$, 3×10^{14}, and 8×10^{14} W cm^{-2}. The RSC probability is defined as the ratio of the RSC yield $\mathbb{Y}$ to the ionized electron yield $N = \int_0^{T_f} dt_0 \int_{-\infty}^{\infty} d^3\mathbf{p}_0\, W(t_0, \mathbf{p}_0)$. The thick solid and dotted curves are our prediction with the GC model $\mathbb{Y}_{\rm GC}/N$ [Eq. (18)], and the SFA $\mathbb{Y}_{\rm SFA}/N$, respectively. The thin curves with stars and crosses are the CTMC simulations of the reference Hamiltonian (1) using $T_p = T$ and $T_p = 8T$, respectively. The filled areas show the estimate of the Coulomb-driven recollision probability for $T_p = 8T$. Red circles show the probability of RSC at the critical ellipticity ξ_c given by Eq. (22).

However, there is a large discrepancy at low ellipticity for low and intermediate intensities, i.e., for $I \lesssim 5 \times 10^{14}$ W cm^{-2}. For such intensities, the rescattering domain where Rydberg states arise is wide compared to the gradient of the ionization rate as observed in the top panel of Figs. 5 and 6(a). As a consequence, the SFA prediction that Rydberg states arise from the center of the rescattering domain is not accurate.

On the contrary, in Fig. 5 we see that the GC model is a good approximation for evaluating the size of the rescattering domain where the Rydberg states are created. In the GC model, a Rydberg state can be created only if the GC energy is negative $\mathcal{E} < 0$. As an approximation, we neglect the cases for which the electron undergoes a Coulomb-driven recollision according to the GC model. The GC prediction of the yield of Rydberg state creation is then given by

$$\mathbb{Y}_{\rm GC} = \int_{\Omega_R} W(t_0, \mathbf{p}_0)\, dt_0 d^3\mathbf{p}_0, \qquad (16)$$

where $\Omega_R = \{t_0 \in [0, T_f], \mathbf{p}_0 \in \mathbb{R}^3 \mid \mathcal{E} < 0\}$ is the set of initial conditions such that the GC energy $\mathcal{E}$ is negative [see Eq. (15)].

According to Sec. IV A, an electron populating the rescattering domain either undergoes a Coulomb-driven recollision or is trapped in a Rydberg state. In order to minimize Coulomb-driven recollisions, we compare the GC prediction with CTMC simulations of the reference model for $T_p = T$. Figure 10 shows the GC prediction of Rydberg state creation probability (solid curves) $\mathbb{Y}_{\rm GC}/N$. We observe an excellent agreement between the results of the simulation of the reference model (1) for $T_p = T$ and the GC prediction for all ellipticities and intensities plotted here. For increasing intensity, the volume of the rescattering domain decreases, as shown in the next section. Hence, at high intensity, the ionization rate varies on large scales compared to the size of the rescattering domain, and the ionization rate is almost constant in the rescattering domain. Therefore, for high intensity, $\mathbb{Y}_{\rm SFA} \propto \mathbb{Y}_{\rm GC}$ as we observe in Fig. 10 for $I = 8 \times 10^{14}$ W cm^{-2}.

V. THE SHAPE OF THE RESCATTERING DOMAIN AND ITS EXPERIMENTAL IMPLICATIONS

A. Analysis of the shape of the rescattering domain

After ionization, the GC energy of the electron is given by Eq. (15). Substituting $\mathbf{A}(t_0) = [\mathbf{A}(t_0)\cdot\hat{\mathbf{n}}_\parallel(t_0)]\hat{\mathbf{n}}_\parallel(t_0) + [\mathbf{A}(t_0)\cdot\hat{\mathbf{n}}_\perp(t_0)]\hat{\mathbf{n}}_\perp(t_0)$ in Eq. (15), the rescattering domain defined by $\mathcal{E} < 0$ is the ensemble of initial conditions $(t_0, \mathbf{p}_0)$ such that

$$[p_\parallel - p_\parallel^\star(t_0)]^2 + [p_\perp - p_\perp^\star(t_0)]^2 + p_{z,0}^2 < \Delta p(t_0)^2, \tag{17}$$

where $\Delta p(t_0) = \sqrt{2|V(\bar{\mathbf{r}}_g(t_0))|}$, $\mathbf{p}_0^\star(t_0) = p_\parallel^\star(t_0)\hat{\mathbf{n}}_\parallel(t_0) + p_\perp^\star(t_0)\hat{\mathbf{n}}_\perp(t_0)$, hence $p_\parallel^\star(t_0) = \mathbf{A}(t_0)\cdot\hat{\mathbf{n}}_\parallel(t_0)$ and $p_\perp^\star(t_0) = \mathbf{A}(t_0)\cdot\hat{\mathbf{n}}_\perp(t_0)$. Here $\bar{\mathbf{r}}_g(t_0) = -\mathbf{E}(t_0)\cosh\tau_0(t_0)/\omega^2$ [see Eq. (7a)]. For a given ionization time t_0, the rescattering domain is a sphere centered at $\mathbf{p}_0^\star(t_0)$ and of radius $\Delta p(t_0)$ in momentum space. The yield of Rydberg state creation in the GC model [see Eq. (16)] becomes

$$\mathbb{Y}_{\rm GC} = \int_0^{T_f} dt_0\, \Delta p(t_0)^3 \int_0^1 d\rho\, \rho^2 \int_0^{2\pi} d\phi \int_0^\pi d\theta\, W(t_0, \mathbf{p}_0^\star(t_0) + \rho\Delta p(t_0)\hat{\mathbf{n}}(t_0,\phi,\theta))\sin\theta, \tag{18}$$

where $\hat{\mathbf{n}}(t_0,\phi,\theta) = \hat{\mathbf{n}}_\parallel(t_0)\cos\phi\sin\theta + \hat{\mathbf{n}}_\perp(t_0)\sin\phi\sin\theta + \hat{\mathbf{z}}\cos\theta$. Equation (18) is used to compute the yield of Rydberg state creation of Fig. 10, and the integrals are performed numerically.

Figures 11(a) and 11(b) show the boundaries of the rescattering domain in the space $(t_0, p_\parallel, p_\perp, p_{z,0} = 0)$ for $\xi = 0.2$ and $\xi = 0.7$. To see how the shape of the rescattering domain evolves as a function of the parameters, we focus on the conditions $p_\parallel = p_{z,0} = 0$ for which the ionization rate is maximum. For low ellipticity, the surface $p_\parallel = p_{z,0} = 0$ and the rescattering domain intersect in approximately ellipsoidal subdomains, while for high ellipticity, they intersect in a band.

1. Close to LP

First, we consider the second order Taylor expansion of the shape of the rescattering domain for $p_\parallel = p_{z,0} = 0$ as a function of the ellipticity in the plane $(t_0, p_\perp)$ close to LP ($\xi \ll 1$). For low ellipticity, the rescattering domain is approximately a set of ellipses, with two subsets: ellipses at the peak laser amplitude (around $\omega t_0 = n\pi$, with $n \in \mathbb{N}$), and ellipses at the lowest laser amplitude [around $\omega t_0 = (n + 1/2)\pi$].

For $p_\parallel = p_{z,0} = 0$, the local minima of the final electron energy [see Eq. (15)] are located at $\omega t_0^\star = n\pi/2$ and $p_\perp^\star = p_\perp^\star(t_0^\star)$ for $n \in \mathbb{N}$. The local minima of the GC energy are the red dots depicted in Fig. 11(c). In Eq. (17) we fix $p_\parallel = p_{z,0} = 0$ and we Taylor expand with respect to $t_0 - t_0^\star$. We obtain that the rescattering domain for $p_\parallel = p_{z,0} = 0$ can be written in the form

$$\frac{(p_\perp - p_\perp^\star)^2}{\Delta p_\perp^2} + \frac{(t_0 - t_0^\star)^2}{\Delta t_0^2} < 1, \tag{19}$$

where terms of order $(t_0 - t_0^\star)^4$ and higher are neglected. Consequently, the subsets of rescattering domain in the plane $(t_0, p_\perp)$ defined by $p_\parallel = p_{z,0} = 0$ are approximately ellipses and are centered around the local minima of the GC energy $(t_0^\star, p_\perp^\star)$. The expressions for $p_\perp^\star$, $\Delta p_\perp$, and Δt_0 depend on whether the ellipse is at the peak laser amplitude or at the lowest laser amplitude.

a. Rescattering domains at the lowest laser amplitude. After Taylor expanding Eq. (17) with respect to t_0 and ξ around the local minima $\omega t_0^\star = (n + 1/2)\pi$ and $\xi = 0$, respectively, one gets (at the third order in the Taylor expansion) $p_\perp^\star \approx (E_0/\omega)(1 - \xi^2/2)$,

$$\Delta p_\perp \approx (E_0/\omega)\xi_c c_\gamma\left(1 - \frac{\xi^2}{4\gamma^2}\right), \qquad \omega\Delta t_0 \approx \xi\, \xi_c c_\gamma,$$

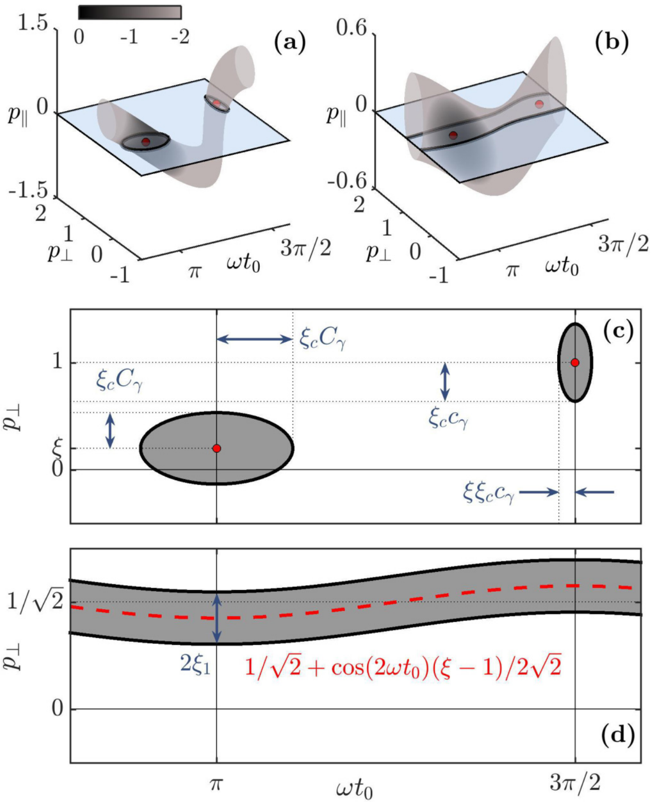

FIG. 11. Shape of the rescattering domain for $I = 8 \times 10^{13}$ W cm^{-2} and $\xi = 0.2$ [close to LP, (a) and (c)], and $\xi = 0.7$ [close to CP, (b) and (d)]. (a) and (b) Boundary of the rescattering domain as a function of the initial conditions $(t_0, p_\parallel, p_\perp, p_{z,0} = 0)$. The color is the logarithm of the PPT ionization rate normalized by its maximum. The black lines are the boundaries of the rescattering domain for $p_\parallel = p_{z,0} = 0$. (c) and (d) Slice of the initial conditions $p_\parallel = p_{z,0} = 0$ [shaded planes in (a) and (b)]. Only the dominant orders in ξ are depicted. The momenta are scaled by E_0/ω.

where $c_\gamma = \sqrt{\gamma}(1+\gamma^2)^{1/4}/\sinh^{-1}\gamma$, ξ_c is defined in Eq. (22), and we have used $\tau \approx \sinh^{-1}\gamma$. Hence, at low ellipticities, the area of these ellipses is proportional to ξ and consequently very small. For LP, the area of these ellipses is zero. In addition, at low ellipticities, these ellipses have a low weight given by the ionization rate, so their influence is negligible.

b. Rescattering domains at the peak laser amplitude. After Taylor expanding Eq. (17) with respect to t_0 and ξ around the local minima $\omega t_0^\star = n\pi$ and $\xi = 0$, respectively, one gets (at the third order in the Taylor expansion) $p_\perp^\star \approx \xi(E_0/\omega)(1-\xi^2/2)$,

$$\Delta p_\perp \approx (E_0/\omega)\xi_c C_\gamma\left[1+\frac{\xi^2}{4(1+\gamma^2)}\right], \tag{20a}$$

$$\omega\Delta t_0 \approx \xi_c C_\gamma\left[1+\xi^2\frac{7+6\gamma^2}{4(1+\gamma^2)}\right], \tag{20b}$$

where $C_\gamma = \gamma/\sinh^{-1}\gamma$ and we have used $\tau \approx \sinh^{-1}\gamma$. Here the area of the ellipses is nonzero for LP, and because these ellipses are highly weighted by the ionization rate, they have a strong influence in the phenomena related to the rescattering domain such as, for instance, Rydberg state creation. We observe that for increasing intensity, these elliptical domains shrink towards their centers for which the GC energy is minimal (red dots in Fig. 11), which correspond also to the SFA conditions for which the electron final energy is zero [see Eq. (14)].

2. *Close to CP*

Next, we consider the second order Taylor expansion of the shape of the rescattering domain for $p_\parallel = p_{z,0} = 0$ as a function of the ellipticity in the plane $(t_0, p_\perp)$ close to CP $(1-|\xi| \ll 1)$. For ellipticity close to 1, the rescattering domain is approximately a band between two lines. We write Eq. (17) in the form

$$p_\perp^-(t_0) < p_\perp < p_\perp^+(t_0),$$

with $p_\perp^\pm(t_0) = p_\perp^\star(t_0) \pm [p_\parallel^\star(t_0)^2 + \Delta p(t_0)^2]^{1/2}$. By Taylor expanding this expression to the first order (the second and third order expansions are too lengthy and do not provide additional relevant information to the discussion) with respect to $1-|\xi|$ around $\xi = 1$, one gets that the lines surrounding the rescattering domain are

$$p_\perp^\pm(t_0) \approx \frac{E_0}{\sqrt{2}\omega}\left[\cos(2\omega t_0)\frac{\xi-1}{2}+1\pm\xi_1\right], \tag{21}$$

where $\xi_1 = (\omega^2/E_0^{3/2})(\gamma^2+1/2)^{-1/4}$ and we have used $\tau \approx \sinh^{-1}\sqrt{2}\gamma$. Hence, Coulomb-driven recollisions and Rydberg state creation after tunneling are likely when the lowest boundary line of the rescattering domain (see Fig. 11) approaches the regions of initial conditions with high ionization rate, i.e., $p_\perp^-(t_0) \lesssim P_\perp$. Fixing $\xi = 1$ and using Eq. (21), one gets

$$E_0^{3/2} \lesssim \omega^2\frac{\sinh^{-1}\gamma}{\gamma(\gamma^2+1/2)^{1/4}}.$$

The term on the right-hand side of the inequality decreases for increasing γ. For $\gamma \ll 1$, the inequality becomes $I \lesssim 2\times10^{13}$ W cm^{-2}. However, the condition $\gamma \ll 1$ implies that $I_p \ll 0.1$ a.u. in order for the electron to undergo a Coulomb-driven recollisions or be trapped in a Rydberg state at this frequency. We observe it is unlikely that the electron undergoes a Coulomb-driven recollision or is trapped in a Rydberg state for nearly CP pulses, if the ionization takes place during the plateau.

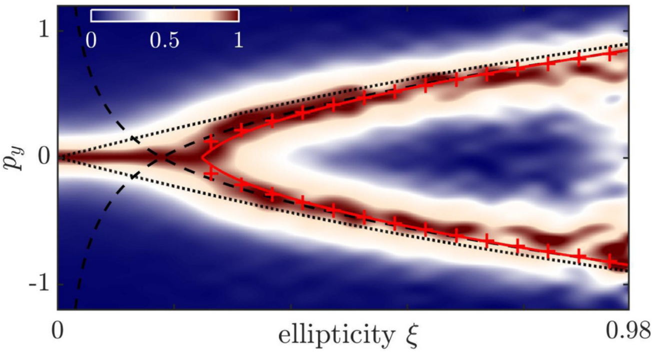

FIG. 12. Photoelectron momentum distribution along the minor polarization axis $\hat{\mathbf{y}}$ as a function of the ellipticity for $I = 1.2\times10^{14}$ W cm^{-2}, Ar ($I_p = 0.58$ a.u.), and $\gamma \sim 1$. The color scale is the experimental data of Ref. [27]. The dotted and dashed black lines are the T trajectory of the SFA and the CCSFA, respectively. The cross markers and red solid lines are the T trajectory of the reference Hamiltonian (1) and the GC model (12), respectively. Momenta are scaled by E_0/ω.

B. Implication of the shape of the rescattering domain

In this section we investigate the physical phenomena related to the shape of the rescattering domain, and we compare the results with experimental data. For instance, when the laser ellipticity ξ varies, the rescattering domain moves in phase space and as a consequence the PMDs change shape. In Fig. 12 we show the experimental measurements from Ref. [27], of the final momentum distribution of the electron along the minor polarization axis $\hat{\mathbf{y}}$ as a function of the ellipticity ξ for $I = 1.2\times10^{14}$ W cm^{-2}, Ar ($I_p = 0.58$ a.u.), and $\gamma \sim 1$. The experimental measurements of the final momentum along the minor polarization axis (color scale) show a distribution peaked around zero for small ellipticity. As the ellipticity increases, we observe a bifurcation of the peak of the distribution at a critical ellipticity $\xi_c \approx 0.25$, for which the distribution is no longer peaked around zero. After the bifurcation (for $\xi > \xi_c$), the peaks of the distribution move further apart for increasing ellipticity. In Ref. [27] a semiclassical theory is developed and is in agreement with the experimental measurements. It is also shown that the initial conditions of the most probable trajectory of the theory in Ref. [27] are relatively close to the initial conditions of the most probable trajectory in PPT. Here we show that this bifurcation can be reproduced and understood by the analysis of the T trajectory only.

In Fig. 12 we also show the $\hat{\mathbf{y}}$ component of the T-trajectory final momentum P_y computed using the SFA $\mathbf{P}^{\mathrm{SFA}} = \hat{\mathbf{y}}\xi(E_0/\omega)\sinh\tau/(\tau\sqrt{\xi^2+1})$ (dotted lines), the CCSFA from Eq. (9) (dashed lines), the reference Hamiltonian (1) (crosses), and the GC prediction [see Eq. (23)] (solid lines). The prediction of the reference Hamiltonian (1) is depicted only if the ionization is direct, i.e., if it has not undergone any recollisions and has not been trapped in Rydberg states. The GC prediction is depicted only when the GC energy is positive. Otherwise, the GC energy is negative and the electron does not reach the detector according to the GC model. We observe an excellent agreement between the experimental results from Ref. [27], the reference Hamiltonian [Hamiltonian (1)], and the GC prediction.

In a nutshell, for $\xi < \xi_c$, the T trajectory is inside the rescattering domain. The GC motion is most often bounded, and as a consequence the electron undergoes recollisions or is trapped in a Rydberg state. When the ellipticity increases, the rescattering domain and the initial conditions of the T trajectory change. At the critical ellipticity ξ_c, the T trajectory is on the boundary of the rescattering domain, i.e., its GC energy is zero. For $\xi > \xi_c$, the GC motion is unbounded, and the electron ionizes without recollision. Therefore, the bunches in the PMDs after the bifurcation (as observed in Fig. 4) are mainly composed of direct ionizations. Right after the bifurcation, a ridge structure can be seen for a certain range of laser parameters and atoms [48,48]. The ridge structure is composed of near-zero-energy electrons induced by rescattering, and the bifurcation with ellipticity can be used to isolate these electrons from the electrons ionized directly [48,50].

1. *Critical ionization time*

In LP fields, for $p_\perp = p_{z,0} = 0$ which reduces to a one-dimensional (1D) model, the SFA predicts that if an electron ionizes after a peak laser amplitude, i.e., at $t_0 > t_0^\star$ ($\omega t_0^\star = n\pi$ where $n \in \mathbb{N}$), it undergoes a recollision [1], while if it ionizes before this peak, i.e., at $t_0 < t_0^\star$, it ionizes directly. In the top panel of Fig. 5 and in Figs. 6(a), 7(a), and 7(b), we observe that this critical time $\omega t_0 = n\pi$ predicted by the SFA is lower if the Coulomb potential is taken into account, and according to the discussion in Sec. IV A, the electron potentially comes back to the ionic core even if it ionizes before the peak of the laser field.

According to the GC model, using Eqs. (19) and (20) for $p_\perp = p_{z,0} = 0$, the left boundaries of the rescattering domain are given by $\omega t_c = n\pi - \xi_c C_\gamma$. If the electron ionizes at $t_0 < t_c$, the electron ionizes directly. If the electron ionizes at $t_0 > t_c$, the electron is in the rescattering domain. According to the discussion in Sec. IV, the electron either populates Rydberg states or undergoes a recollision. In particular, if an electron ionizes before the peak of the laser field and recollides, it is mainly because of the Coulomb interaction and the bounded motion of its GC that brings the electron back to the core. If the electron ionizes after the peak of the laser field, its GC initial radial momentum is negative (and its angular momentum is zero in 1D), and as a consequence the electron recollides.

The same arguments are extended to estimate t_c for low ellipticity and $\xi \leqslant \xi_c$. We fix the initial momentum at its most probable value given by ($p_\parallel = P_\parallel$, $p_\perp = P_\perp$, $p_{z,0} = P_{z,0}$) and we let the ionization time t_0 free. At low ellipticity $P_\parallel = P_{z,0} = 0$ and $P_\perp \approx 0$, and if $\omega t_0 = \omega t_0^\star$ the trajectory is approximately at the center of the rescattering domain [see Fig. 11(c)]. As a consequence, there exist intervals of ionization time t_0 for which the initial conditions are inside the rescattering domain, but also because of the shape of the rescattering domain [see Fig. 11(c)], there are intervals of ionization times t_0 for which the initial conditions are outside the rescattering domain. The critical time t_c is the ionization time for which $(t_c, P_\parallel, P_\perp, P_{z,0})$ is on the left boundary of the rescattering domain. In Eq. (19) we transform the inequality into an equality and we fix $p_\perp = P_\perp \approx \xi(E_0/\omega)(1 - \gamma/\sinh^{-1}\gamma)$ [see Eq. (4b)]. Then, using Eqs. (20) up to the second order in ξ, the critical time t_c is given by

$$\omega t_c \approx \omega t_0^\star - C_\gamma\sqrt{\xi_c^2 - \xi^2},$$

with $C_\gamma = \gamma/\sinh^{-1}\gamma$ and ξ_c defined Eq. (22). Also, we have seen in Sec. IV that if the ionization takes place after the peak of the laser field, the GC radial momentum is negative and the electron tends to recollide with the ionic core. Hence, the ionization time t_0 for direct ionization is $\omega t_0 \in [\omega t_c, \omega t_c - \pi/2]$. This is in agreement with the CTMC simulations of Ref. [51].

2. *Critical ellipticity*

Next, we consider the bifurcation with respect to the laser parameters. We consider the T trajectory given by the initial conditions (4) and $\omega t_0 = \pi$. For LP ($\xi = 0$), the T trajectory is inside the rescattering domain. As a consequence, the GC energy of the T trajectory is negative, and the electron is either trapped in a Rydberg state, or undergoes a recollision. For increasing ellipticity, $p_\perp^\star(t_0)$ increases and $P_\perp$ decreases. At ellipticity $\xi = \xi_c$, the initial condition of the T trajectory ($\omega t_0 = \pi$, $p_\parallel = P_\parallel$, $p_\perp = P_\perp$, $p_{z,0} = P_{z,0}$) crosses the boundary of the rescattering domain. In Eq. (19) we substitute the initial conditions of the T trajectory $\omega t_0 = \pi$ and $p_\perp = P_\perp \approx \xi(E_0/\omega)\gamma/\sinh^{-1}\gamma$ [see Eq. (4b)] and we use Eq. (20) up to the first order in ξ. Replacing ξ by ξ_c and assuming that $\xi_c^2 \ll 1$, the critical ellipticity is

$$\xi_c \approx \frac{\sqrt{2}\omega^2}{E_0^{3/2}} \frac{\sinh^{-1}\gamma}{\gamma(1+\gamma^2)^{1/4}}, \tag{22}$$

(see Supplemental Material of Ref. [24] for a detailed derivation). For $\xi > \xi_c$, the GC energy of the T trajectory is positive and its motion is unbounded. The T trajectory ionizes directly, i.e., it does not experience rescattering. This corresponds to a direct ionization. Indeed, in Fig. 10 we observe that for $\xi > \xi_c$, the probability of Rydberg state creation and Coulomb-driven recollisions decreases significantly for increasing ellipticity.

Hence, for $\xi > \xi_c$, the GC motion is unbounded and the electron is driven to the detector. The initial condition of the GC of the T trajectory is determined by combining Eqs. (7) and (4), and reads

$$\mathbf{R}_{g,0} = \hat{\mathbf{x}}\frac{E_0}{\omega^2\sqrt{\xi^2+1}}\cosh\tau,$$

$$\mathbf{P}_{g,0} = \hat{\mathbf{y}}\frac{\xi E_0}{\omega\sqrt{\xi^2+1}}\frac{\sinh\tau}{\tau}.$$

Since Hamiltonian (12) is time independent and rotationally invariant, the GC energy $\mathcal{E}_T$ and angular momentum $\ell_T = \hat{\mathbf{z}} \cdot \mathbf{R}_{g,0} \times \mathbf{P}_{g,0}$ of the T trajectory are conserved and given by

$$\mathcal{E}_T = \frac{\xi^2 E_0^2}{2\omega^2(\xi^2+1)} \frac{\sinh^2 \tau}{\tau^2} - \frac{\omega^2\sqrt{\xi^2+1}}{E_0 \cosh \tau},$$

$$\ell_T = \frac{\xi E_0^2}{\omega^3(\xi^2+1)} \frac{\sinh 2\tau}{2\tau},$$

with $V(\mathbf{R}_{g,0}) \approx -1/|\mathbf{R}_{g,0}|$. When the electric field is turned off, we assume that the final momentum of the T trajectory and the final momentum of its GC are equal, with $P_x = \sqrt{2\mathcal{E}_T}\cos\Theta$ and $P_y = \sqrt{2\mathcal{E}_T}\sin\Theta$, where its scattering angle is given by [see Eq. (B3)]

$$\Theta = \pi/2 + \sin^{-1}\left(2\mathcal{E}_T \ell_T^2 + 1\right)^{-1/2}.$$

As a consequence,

$$P_x = -\sqrt{2\mathcal{E}_T}\left(2\mathcal{E}_T \ell_T^2 + 1\right)^{-1/2}, \tag{23a}$$

$$P_y = \sqrt{2\mathcal{E}_T}\left[1 - \left(2\mathcal{E}_T \ell_T^2 + 1\right)^{-1}\right]^{1/2}. \tag{23b}$$

Equations (23) are used to compute P_x and P_y of the GC. In the PMDs we recall that the bifurcation in P_x signals the appearance of Coulomb asymmetry as a function of the ellipticity, while the bifurcation in P_y shows the breakdown of Coulomb focusing as a function of the ellipticity. We observe that Coulomb asymmetry appears at the same time as Coulomb focusing begins to recede. Close to the bifurcation, for $\xi \approx \xi_c$ and using $\tau \approx \sinh^{-1}\gamma$, one has

$$\mathcal{E}_T \approx (\xi - \xi_c) 4U_p \xi_c (\gamma / \sinh^{-1}\gamma)^2, \tag{24a}$$

$$P_x \approx -(\xi - \xi_c)^{1/2}\sqrt{2\xi_c}(E_0/\omega)(\gamma/\sinh^{-1}\gamma), \tag{24b}$$

$$P_y \approx (\xi - \xi_c) 2\sqrt{2}(E_0/\omega)(\gamma/\sinh^{-1}\gamma), \tag{24c}$$

where $U_p = E_0^2/4\omega^2$ is the ponderomotive energy (see Ref. [24] for more details). As a consequence, the critical exponents of the bifurcation predicted by the GC model for P_x and P_y are 0.5 and 1, respectively, i.e., $P_x \sim (\xi - \xi_c)^{1/2}$ and $P_y \sim (\xi - \xi_c)$. We observe that close to the bifurcation and for increasing ellipticity, the Coulomb asymmetry measured by the bifurcation in P_x increases faster than the breakdown of Coulomb focusing measured by the bifurcation in P_y.

3. Comparison with experiments

In Fig. 13 we show the final momentum of the T-trajectory $\mathbf{P}$ as a function of the ellipticity ξ computed using the SFA (dotted lines), the CCSFA from Eq. (9) (dashed lines), the reference Hamiltonian (1) (crosses), and the GC from Eqs. (23) (solid lines). The T-trajectory final momentum of the reference Hamiltonian (1) is not depicted if it is trapped in a Rydberg state or undergoes rescattering. In the lower-left panel, the hexagrams are the experimental data of $\mathbf{P}$ reproduced from Ref. [18].

For $I = 8 \times 10^{13}$ W cm^{-2}, He ($I_p = 0.9$ a.u.), and $\gamma \sim 0.6$ (top panels of Fig. 13), the T trajectory of the reference Hamiltonian (1) corresponds to a direct ionization at the critical ellipticity $\xi_c \approx 0.25$, and reaches the detector without undergoing rescattering for $\xi > \xi_c$. The critical ellipticity is in agreement with the prediction $\xi_c \approx 0.26$ of Eq. (22). On the left panel, we observe a good agreement between the T-trajectory final momentum $\mathbf{P}$ of the reference Hamiltonian (1) (thin curves with crosses) and that of the GC model (thick solid curves) for the entire range of ellipticities $\xi > \xi_c$.

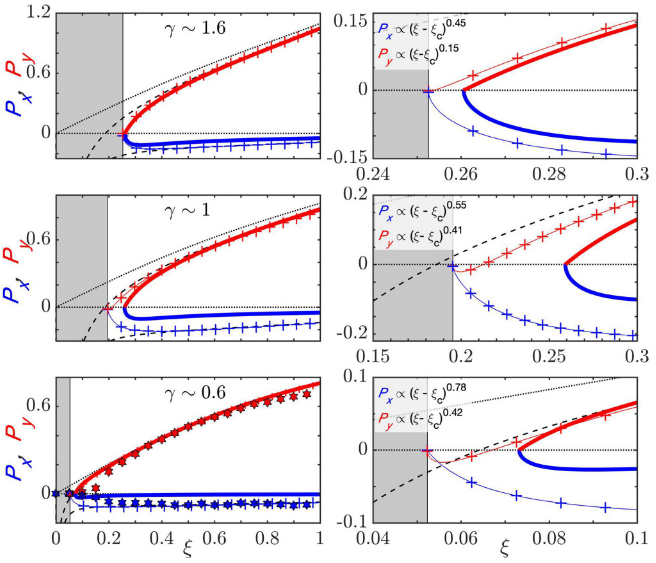

FIG. 13. Final momentum of the T-trajectory $\mathbf{P} = P_x\hat{\mathbf{x}} + P_y\hat{\mathbf{y}}$ as a function of the ellipticity ξ. Top panels: $I = 8 \times 10^{13}$ W cm^{-2}, He ($I_p = 0.9$ a.u.), and $\gamma \sim 1.6$. Middle panels: $I = 1.2 \times 10^{14}$ W cm^{-2}, Ar ($I_p = 0.58$ a.u.), and $\gamma \sim 1$. Bottom panels: $I = 8 \times 10^{14}$ W cm^{-2}, He ($I_p = 0.9$ a.u.), and $\gamma \sim 0.6$. The hexagrams are the experimental data reproduced from Ref. [18]. In all panels: the dotted and dashed black lines are the T trajectory of the SFA and the CCSFA, respectively. The thin (with crosses) and solid curves are the T trajectory of the reference Hamiltonian (1) and the GC model (12), respectively. The components of the final momentum of the T-trajectory P_x and P_y are depicted in blue (lower line) and red (upper line), respectively. The critical ellipticity ξ_c is at the intersection between the gray and white regions and corresponds to the largest ellipticity for which the T trajectory of the reference Hamiltonian (1) is negative. The right panels are zooms of the left panels in the neighborhood of the critical ellipticity. We indicate the scaling of $\mathbf{P}$ of the reference model (1) in the neighborhood of the bifurcation. The momenta are scaled by E_0/ω.

For $I = 1.2 \times 10^{14}$ W cm^{-2}, Ar ($I_p = 0.58$), and $\gamma \sim 1$ (middle panels of Fig. 13), the T trajectory of the reference Hamiltonian (1) becomes a direct ionization at $\xi_c \approx 0.19$ while the GC prediction [see Eq. (22)] is $\xi_c \approx 0.24$. There is a small disagreement between the critical ellipticity of the reference model and the prediction of Eq. (22). However, there is a good agreement of the GC critical ellipticity with the experimental measurements of Ref. [27] of $\xi_c \approx 0.24$ as observed in Fig. 12. Furthermore, there is a good agreement between the T-trajectory final momentum $\mathbf{P}$ of the reference Hamiltonian (1) (thin curves with crosses) and that of the GC model (thick solid curves) for $\xi \gtrsim 0.3$. However, we observe a small disagreement between P_x of the reference Hamiltonian (1) (thin curves with crosses) and the GC prediction for all ellipticities. This discrepancy is related to the observations made in Fig. 2 and whose origin is discussed below.

For $I = 8 \times 10^{14}$ W cm^{-2}, He ($I_p = 0.9$), and $\gamma \sim 0.6$ (lower panels of Fig. 13), the T trajectory of the reference

Hamiltonian (1) becomes a direct electron at $\xi_c \approx 0.05$. The critical ellipticity is in agreement with the prediction $\xi_c \approx 0.07$ of Eq. (22). In addition, these values agree well with the critical ellipticity $\xi_c \approx 0.08$ of the experiments [18] (hexagrams). There is again a good agreement between the T-trajectory final momentum $\mathbf{P}$ of the reference Hamiltonian (1) (thin curves with crosses) and that of the GC model (thick solid curves) for $\xi \gtrsim 0.1$. However, we observe a disagreement between P_x of the reference Hamiltonian (1) (thin curves with crosses) and the GC prediction in the entire ellipticity range. We notice that for decreasing Keldysh parameters, the disagreement between P_x of the reference Hamiltonian (1) and the GC model increases, as observed in the lower panel of Fig. 2.

On the right panels of Fig. 13 we observe a good agreement between the exponents of P_x of the reference Hamiltonian (1) at the bifurcation and the prediction 0.5 of Eq. (24). However, the exponent of P_y at the bifurcation is much smaller than the exponent 1 predicted by Eq. (24).

In the left panels of Fig. 13 we observe excellent agreement between the T-trajectory final momentum of the reference Hamiltonian (1) (thin curves with crosses) and that of the CCSFA (dashed curves) after the bifurcation when the electron final energy is large.

4. T-trajectory analysis

Here we show that the origin of the disagreements between the T trajectory of the reference Hamiltonian (1) and the GC T trajectory—the disagreement of P_x for small Keldysh parameters, or the disagreement with the critical exponents of P_y in the neighborhood of the bifurcation—are related to an underestimate of the Coulomb interaction by the GC model for a short time after ionization. In contrast, we show that the CCSFA agrees well with the solution of the reference Hamiltonian (1) for $\xi \gg \xi_c$ while it cannot capture correctly the phenomena related to the bifurcation.

In Fig. 14 the red dash-dotted, cyan (light gray) solid, and black dashed curves are the T trajectory of Hamiltonian (6), the GC model (12), and the CCSFA given by Eqs. (9), respectively. The thick dark blue (dark gray) curves are the T trajectory of the reference Hamiltonian (1). Associated with each trajectory, we also show the GC energy, for each model, as a function of time per laser cycle t/T. The GC energy for each model consists in substituting the solution $(\mathbf{r}_g(t), \mathbf{p}_g(t))$ for each model in the GC Hamiltonian (12), i.e., $\bar{H}(\mathbf{r}_g(t), \mathbf{p}_g(t))$. Where the GC energy of the reference model is conserved, the GC model (whose GC energy is conserved) is valid [25].

For $\gamma \sim 1.6$ [see Figs. 14(a)–14(d)], the electron ionizes far from the ionic core ($|\mathbf{r}_0| \sim E_0/\omega^2$). For $\xi = 0.25$ and $\xi = 0.7$, respectively, we see the variations of the GC energy of the T trajectory of Hamiltonian (6) (dash-dotted curve) are small, a signature of the validity of the GC model and an absence of rescattering. When the GC energy of Hamiltonian (6) becomes constant, it is only about 0.02 a.u. above the GC model prediction. As a consequence, we observe a good agreement between the trajectories of Hamiltonian (6) and the GC model trajectories in Figs. 14(a) and 14(b). In particular, at $\xi = 0.25$, we observe the T trajectory of Hamiltonian (6) is trapped in a Rydberg state, a feature which is reproduced by the GC model [cyan (light gray) solid curve], but not well reproduced by the CCSFA (dashed black curve). Indeed, the Coulomb interaction remains significant for a long time after ionization during Rydberg state creation, and the conditions for the validity of the CCSFA are not met.

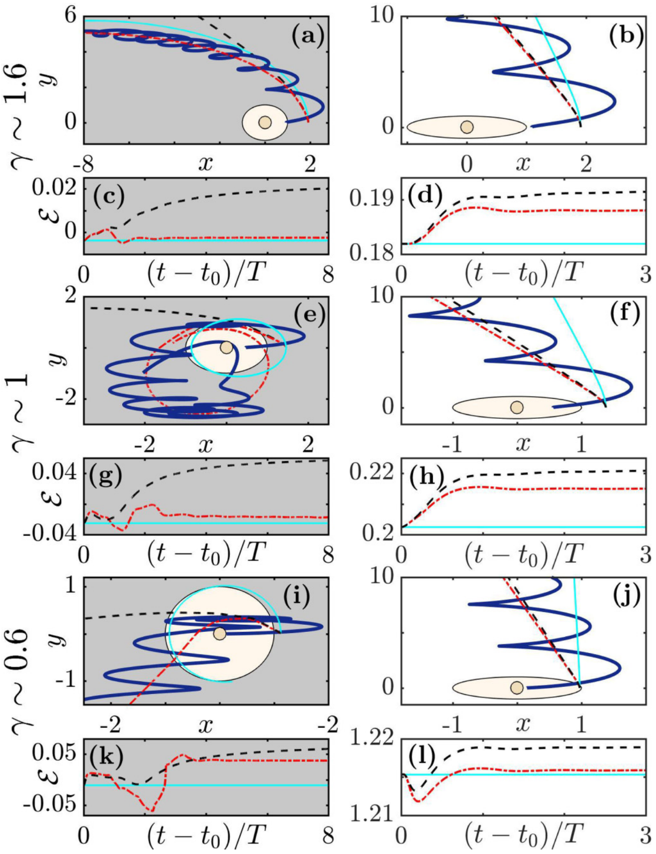

FIG. 14. (a), (b), (e), (f), (i), and (j) T trajectory in the polarization plane (x, y). The thick dark blue (dark gray) curves are the T trajectory of the reference Hamiltonian (1). The red dash-dotted, cyan (light gray) solid, and dashed black curves are the T trajectory of Hamiltonian (6), the GC model (12), and the CCSFA (9), respectively. (c), (d), (g), (h), (k), and (l) Energy (12) as a function of $(t - t_0)/T$, with $t_0 = T/2$, associated with each model. Right panels: $\xi = 0.7$. (a) and (c), (e) and (g), and (i) and (k) (the gray background panels are those for $\xi < \xi_c$) $\xi = 0.25$, $\xi = 0.15$, and $\xi = 0.05$, respectively. (a)–(d) $I = 8 \times 10^{13}$ W cm^{-2}, He ($I_p = 0.9$ a.u.), and $\gamma \sim 1.6$ (same parameters as the top panels of Fig. 13). (e)–(h) $I = 1.2 \times 10^{14}$ W cm^{-2}, Ar ($I_p = 0.58$ a.u.), and $\gamma \sim 1$ (same parameters as the middle panels of Fig. 13). (i)–(l) $I = 8 \times 10^{14}$ W cm^{-2}, He ($I_p = 0.9$ a.u.), and $\gamma \sim 0.6$ (same parameters as the lower panels of Fig. 13). The dots indicate the origin, and the circles $|\mathbf{r}| = E_0/\omega^2$. The distances are scaled by E_0/ω^2, the energy is in a.u.

For $\gamma \sim 1$ [see Figs. 14(e)–14(h)], the electron ionizes closer to the ionic core ($|\mathbf{r}_0| \sim 0.4E_0/\omega^2$). For $\xi = 0.15$, the electron T trajectory of Hamiltonian (6) (dash-dotted curve) and the GC model are trapped in Rydberg states. However, there is a large discrepancy between the trajectories. Indeed, in Fig. 14(g) we observe that the dash-dotted red curve varies after ionization, indicating that the electron rescatters for a short time after ionization [25]. For $\xi = 0.7$, the same happens in terms of energy [see Fig. 14(h)], and we see that the GC trajectory does not agree well with the T trajectory of Hamiltonian (6) [see Fig. 14(f)]. When the energy of Hamiltonian (6) becomes constant at $t \approx T/2$, it is larger than the GC energy prediction of 0.15 a.u. In Fig. 14(e) or 14(f) we observe that after ionization, the initial electron distance from the core is $|\mathbf{r}_0| \sim 0.4E_0/\omega^2$, while the GC initially at a distance $|\mathbf{r}_{g,0}| \sim 1.4E_0/\omega^2$ from core. Since in the GC model, the Coulomb interaction is evaluated at the GC position only, when the electron is closer to the core than predicted by the GC model, as is the case after ionization for $\gamma \lesssim 1.6$, the Coulomb interaction is underestimated in the GC model: the closer the electron to the ionic core, the more underestimated the Coulomb interaction.

For $\gamma \sim 0.6$ [see Figs. 14(i)–14(l)], the electron ionizes even closer to the ionic core ($|\mathbf{r}_0| \sim 0.15E_0/\omega^2$). For $\xi = 0.05$ and $\xi = 0.07$, there are also discrepancies between the cyan (light gray) and red curves. We observe that the energy of the T trajectory of Hamiltonian (6) [red dash-dotted curve in Figs. 14(k) and 14(l)] varies a lot for a short time after ionization (about $0.2T$). Here again, the electron rescatters after ionization. In Fig. 14(l), when the red dash-dotted curve becomes constant, the energy is above the GC prediction only by 0.02 a.u. However, this agreement is only coincidental since the T trajectories of Hamiltonian (6) and of the GC disagree significantly due to the increase in energy of the rescattering. We observe that this increase in energy after ionization is well captured by the CCSFA.

In each panel we observe an excellent agreement between the CCSFA and the T trajectory of Hamiltonian (6) for a short time after ionization, i.e., $0 < t - t_0 \lesssim T$, when the hypotheses of the CCSFA are met. This method is effective for short timescale dynamics or phenomena [37,38,48]. This agreement persists for longer times if the electron leaves quickly the ionic core region like in Ref. [17] or for large ellipticity (see Sec. III A), i.e., if its drift momentum is initially large.

VI. CONCLUSIONS

In this article we have investigated the role of the Coulomb potential in atoms subjected to strong laser fields. To do so, we have considered three reduced models of the reference Hamiltonian (1), namely the SFA [Eqs. (8)], the CCSFA [Eqs. (9)], and the GC model [Eqs. (12)]. The analysis of these three reduced models allowed us to shed light on the manifestations of the Coulomb potential in various ionization processes. In the SFA, there are two types of trajectories: subcycle recollisions and direct ionizations. However, even when the intensity is very large, i.e., when the conditions of the SFA are met, the Coulomb interaction still makes its presence known for long timescale phenomena. In particular, even at very high intensities, the Coulomb asymmetry persists as seen in Fig. 2 and discussed in Sec. III A. The Coulomb interaction brings with it a variety of additional types of trajectories, such as Coulomb-driven recollisions and Rydberg states. We have shown in Sec. IV that these two processes are intimately related, and can be interpreted and predicted by the GC model.

During step (ii) of the recollision scenario, we have shown that the electron oscillates around the GC trajectory. In phase space, the GC trajectory lies on a curve of constant energy $\mathcal{E} = \bar{H}(\bar{\mathbf{r}}_g, \bar{\mathbf{p}}_g)$. If $\mathcal{E} > 0$, the GC motion is unbounded. In this case, it is likely the electron recollides if its GC angular momentum is near zero and its initial radial momentum is negative [like in Fig. 6(b)]. Otherwise, the electron ionizes directly without recollision [like in Fig. 6(c)]. If $\mathcal{E} < 0$, the GC motion is bounded. In this case, there exists at least one time at which the electron turns back towards the ionic core. Then, the electron passes by the ionic core before the laser field is turned off and may or may not recollide. If the electron does recollide [like in Figs. 6(d) and 7(d)], the GC energy jumps to a new energy level, as described in Ref. [25]. If the laser field is turned off before the electron recollides [as in Figs. 6(e) and 7(e)], the electron ends up in a Rydberg state.

The GC model does not capture the rescattering effects close to the ionic core but the CCSFA can since it is a rather short timescale phenomenon [37,39,40,48]. As observed in Fig. 14, the variations of energy of the reference model (1) can be well described by the CCSFA for short timescales. After rescattering, the electron potentially ionizes if its GC energy becomes positive [such as in Fig. 6(d)]. Therefore, the CCSFA and the GC models are clearly complementary. The CCSFA is adapted for describing short timescale processes such as rescattering while the GC model is more suited for describing long timescale processes such as Coulomb-driven recollisions and the creation of Rydberg states.

ACKNOWLEDGMENTS

We thank Jan-Michael Rost, Ulf Saalmann, François Mauger, and Cornelia Hoffman for helpful discussions, and Ursula Keller, Yunquan Liu, and their groups for sharing their experimental results with us. The project leading to this research has received funding from the European Union's Horizon 2020 research and innovation program under the Marie Skłodowska-Curie Grant agreement No. 734557. T.U. and S.A.B. acknowledges funding from the NSF (Grant No. PHY1602823).

APPENDIX A: IONIZATION RATE

Throughout this article we use the nonadiabatic ionization rate given by the Perelomov-Popov-Terent'ev [31] formulas, rewritten in a different form in Ref. [41]. We denote $\gamma_0(t_0) = \omega\sqrt{2I_p}/|\mathbf{E}(t_0)|$. The initial position of the electron is parametrized by the ionization time t_0 and its initial momentum is written as $\mathbf{p}_0 = p_\parallel \hat{\mathbf{n}}_\parallel(t_0) + p_\perp \hat{\mathbf{n}}_\perp(t_0) + p_{z,0}\hat{\mathbf{z}}$ for a polarization plane $(\hat{\mathbf{x}}, \hat{\mathbf{y}})$. The PPT ionization rate [31] reads

$$\begin{aligned} W(t_0, \mathbf{p}_0) &\\ \propto \frac{h(\gamma_0(t_0), \xi)}{|\mathbf{E}(t_0)|} &\exp\left[-\frac{2I_p}{\omega} g(\gamma_0(t_0), \xi)\right] \\ \times \exp&\left\{-\frac{1}{\omega}\left[c_\parallel p_\parallel^2 + c_\perp\left(p_\perp - p_{\perp,0}^{\max}\right)^2 + c_z p_{z,0}^2\right]\right\}, \end{aligned} \tag{A1}$$

where the functions g and h are

$$g(\gamma_0,\xi) = \left(1+\frac{1+\xi^2}{2\gamma_0^2}\right)\tau_0 - (1-\xi^2)\frac{\sinh 2\tau_0}{4\gamma_0^2} - \xi^2\frac{\sinh^2\tau_0}{\gamma_0^2\tau_0},$$
$$h(\gamma_0,\xi) = \frac{2\sigma\gamma_0}{\sinh 2\tau_0},$$

with the notation

$$\sigma = \left(1-\xi^2+\xi^2\frac{\tanh\tau_0}{\tau_0}\right)^{-1}.$$

The coefficients $c_\parallel$, $c_\perp$, and c_z, which are inversely proportional to the square of the standard deviation of the distribution along the longitudinal and transverse momentum, are given by

$$c_\parallel = \tau_0 - \sigma\tanh\tau_0,$$
$$c_\perp = \tau_0 + \sigma\xi^2\frac{(\tau_0-\tanh\tau_0)^2}{\tau_0^2\tanh\tau_0},$$
$$c_z = \tau_0.$$

The coefficients satisfy $c_\parallel > c_\perp$, implying that the distributions are more spread out along the transverse direction than along the longitudinal direction. The most probable initial transverse momentum $p_{\perp,0}^{\max}$ is

$$p_{\perp,0}^{\max} = \frac{\xi E_0}{\omega\sqrt{\xi^2+1}}\left(1-\frac{\sinh\tau_0}{\tau_0}\right),$$

for a transverse unitary vector defined as $\hat{\mathbf{n}}_\perp(t_0) = -[\hat{\mathbf{n}}_\parallel(t_0)\cdot\hat{\mathbf{y}}]\hat{\mathbf{x}} + [\hat{\mathbf{n}}_\parallel(t_0)\cdot\hat{\mathbf{x}}]\hat{\mathbf{y}}$.

APPENDIX B: FINAL MOMENTUM OF THE ELECTRON IN THE GC MODEL

In the GC model given in Eq. (12), the energy and the angular momentum are conserved for rotationally invariant potentials. The model is accurate far from the core, and as a consequence we assume that $V(\bar{\mathbf{r}}_g) = -Z/|\bar{\mathbf{r}}_g|$ with Z an effective charge. The Hamiltonian reads

$$\bar{H}_g(\bar{\mathbf{r}}_g,\bar{\mathbf{p}}_g) = \frac{|\bar{\mathbf{p}}_g|^2}{2} - \frac{Z}{|\bar{\mathbf{r}}_g|}.$$

In this model the guiding-center motion is planar due to the conservation of the angular momentum. We perform the polar-nodal canonical transformation [52] $(\bar{\mathbf{r}}_g,\bar{\mathbf{p}}_g)\mapsto(r,\theta,\nu,p_r,p_\theta,p_\nu)$,

$$\bar{\mathbf{r}}_g = r\mathbf{Q}\hat{\mathbf{x}}, \quad \bar{\mathbf{p}}_g = \mathbf{Q}(\hat{\mathbf{x}}p_r + \hat{\mathbf{y}}p_\theta/r),$$

where the total rotation matrix is $\mathbf{Q} = \mathbf{R}_\nu\mathbf{R}_i\mathbf{R}_\theta$, with

$$\mathbf{R}_\theta = \begin{bmatrix}\cos\theta & -\sin\theta & 0\\ \sin\theta & \cos\theta & 0\\ 0 & 0 & 1\end{bmatrix},$$
$$\mathbf{R}_\nu = \begin{bmatrix}\cos\nu & -\sin\nu & 0\\ \sin\nu & \cos\nu & 0\\ 0 & 0 & 1\end{bmatrix},$$
$$\mathbf{R}_i = \begin{bmatrix}1 & 0 & 0\\ 0 & \cos i & -\sin i\\ 0 & \sin i & \cos i\end{bmatrix},$$

where $\cos i = p_\nu/p_\theta$, $\sin i = [1-(p_\nu/p_\theta)^2]^{1/2}$. The GC Hamiltonian for the hard Coulomb potential becomes

$$\bar{H}_g(r,\theta,\nu,p_r,p_\theta,p_\nu) = \frac{p_r^2}{2} + \frac{p_\theta^2}{2r^2} - \frac{Z}{r}. \tag{B1}$$

In order to compute the asymptotic configuration of the guiding center with Hamiltonian (B1), one needs to determine the initial conditions in the polar-nodal coordinates as a function of the initial conditions in the Cartesian coordinates. The momenta are given by $p_r = \bar{\mathbf{p}}_g\cdot\bar{\mathbf{r}}_g/|\bar{\mathbf{r}}_g|$, $p_\theta = |\mathbf{L}|$, and $p_\nu = \mathbf{L}\cdot\hat{\mathbf{z}}$, with $\mathbf{L} = \bar{\mathbf{r}}_g\times\bar{\mathbf{p}}_g$. The distance from the origin is $r = |\bar{\mathbf{r}}_g|$. Concerning the angles, we first introduce the unitary vectors

$$\hat{\mathbf{n}}_1 = \begin{cases}\hat{\mathbf{x}} & \text{if } \hat{\mathbf{z}}\times\mathbf{L} = \mathbf{0},\\ \hat{\mathbf{z}}\times\mathbf{L}/|\hat{\mathbf{z}}\times\mathbf{L}| & \text{otherwise,}\end{cases}$$

and $\hat{\mathbf{n}}_2 = \mathbf{L}/|\mathbf{L}|\times\hat{\mathbf{n}}_1$. The angles θ and ν as a function of the Cartesian coordinates are given by

$$\cos\theta = \hat{\mathbf{n}}_1\cdot\bar{\mathbf{r}}_g/|\bar{\mathbf{r}}_g|, \quad \sin\theta = \hat{\mathbf{n}}_2\cdot\bar{\mathbf{r}}_g/|\bar{\mathbf{r}}_g|,$$

and

$$\cos\nu = \hat{\mathbf{n}}_1\cdot\hat{\mathbf{x}}, \quad \sin\nu = \hat{\mathbf{n}}_1\cdot\hat{\mathbf{y}}.$$

If $\hat{\mathbf{z}}\times\mathbf{L} = \mathbf{0}$, $\sin i = 0$, and as a consequence the angle of rotation is $\theta+\nu$. By fixing $\hat{\mathbf{n}}_1 = \hat{\mathbf{x}}$ in this case, we choose arbitrary $\nu = 0$ in order to be consistent with the definition of θ and ν.

The energy $\mathcal{E} = \bar{H}_g(r,\theta,\nu,p_r,p_\theta,p_\nu)$, the angular momentum p_θ, ν, and p_ν are clearly constants of the motion. If $\mathcal{E} < 0$, the electron motion is bounded. The two turning points at which the electron radial momentum changes sign are the perihelion r_- (closest distance of the orbit from the core) and the aphelion r_+ (largest distance of the orbit from the core) such that

$$r_\pm = \frac{Z}{2|\mathcal{E}|}\left(1\pm\sqrt{1-2p_\theta^2|\mathcal{E}|/Z^2}\right). \tag{B2}$$

If $\mathcal{E} > 0$, the GC trajectory is unbounded and the electron reaches the detector. The asymptotic configuration (when r goes to infinity) is given by $p_r = \sqrt{2\mathcal{E}}$. Concerning the final scattering angle θ, if $p_\theta = 0$, $\theta = \theta_0$ (if $p_{r,0} > 0$) and $\theta_0 + \pi$ (if $p_{r,0} < 0$). If $p_\theta \neq 0$, the final scattering angle is given by

$$\theta = \begin{cases}\theta_0 + \sin^{-1}u_0 + \sin^{-1}\beta & \text{if } p_{r,0} > 0,\\ \theta_0 + \pi/2 + \sin^{-1}\beta & \text{if } p_{r,0} = 0,\\ \theta_0 + \pi - \sin^{-1}u_0 + \sin^{-1}\beta & \text{if } p_{r,0} < 0,\end{cases} \tag{B3}$$

with $u_0 = \beta[p_\theta^2/(Zr_0) - 1]$, $\beta = (2\mathcal{E}p_\theta^2/Z^2 + 1)^{-1/2}$, and $r_0 = |\bar{\mathbf{r}}_{g,0}|$. Finally, the final momentum of the GC in the Cartesian coordinates is given by

$$\bar{\mathbf{p}}_g = p_r\mathbf{Q}\hat{\mathbf{x}}.$$

We notice that in the two-dimensional case where the dynamics is in the polarization plane $(\hat{\mathbf{x}},\hat{\mathbf{y}})$, we have $\mathbf{L}\times\hat{\mathbf{z}} = \mathbf{0}$. Therefore, $|p_\theta| = |p_\nu|$, $\sin i = 0$, and $\mathbf{R}_\nu$ is the identity matrix. Therefore, in this case, the final momentum reads $\bar{\mathbf{p}}_g = p_r(\hat{\mathbf{x}}\cos\theta + \hat{\mathbf{y}}\sin\theta\cos i)$, where $\cos i = +1$ (-1) for $p_\nu > 0$ (<0).

[1] P. B. Corkum, Phys. Rev. Lett. **71**, 1994 (1993).
[2] W. Becker, F. Grabson, R. Kopold, and D. B. Milošević, Adv. At. Mol. Opt. Phys. **48**, 35 (2002).
[3] P. B. Corkum and F. Krausz, Nature Phys. **3**, 381 (2007).
[4] P. Agostini and L. F. DiMauro, Contemp. Phys. **49**, 179 (2008).
[5] F. Krausz and M. Ivanov, Rev. Mod. Phys. **81**, 163 (2009).
[6] W. Becker, X. J. Liu, P. J. Ho, and J. H. Eberly, Rev. Mod. Phys. **84**, 1011 (2012).
[7] M. Meckel, D. Comtois, D. Zeidler, A. Staudte, D. Pavičić, H. C. Bandulet, H. Pépin, J. C. Kieffer, R. Dörner, D. M. Villeneuve, and P. B. Corkum, Science **320**, 1478 (2008).
[8] K. J. Gaffney and H. N. Chapman, Science **316**, 1444 (2007).
[9] L.-Y. Peng, W.-C. Jiang, J.-W. Geng, W.-H. Xiong, and Q. Gong, Phys. Rep. **575**, 1 (2015).
[10] C. I. Blaga, J. Xu, A. D. DiChiara, E. Sistrunk, K. Zhang, P. Agostini, T. A. Miller, L. F. DiMauro, and C. D. Lin, Nature (London) **483**, 194 (2012).
[11] E. Goulielmakis, Z.-H. Loh, A. Wirth, R. Santra, N. Rohringer, V. S. Yakovlev, S. Zherebtsov, T. Pfeifer, A. M. Azzeer, M. Kling, S. R. Leone, and F. Krausz, Nature (London) **466**, 739 (2010).
[12] L. V. Keldysh, Zh. Eksp. Teor. Fiz. **47**, 1945 (1965) [Sov. Phys. JETP **20**, 1307 (1965)].
[13] K. J. Schafer, B. Yang, L. F. DiMauro, and K. C. Kulander, Phys. Rev. Lett. **70**, 1599 (1993).
[14] M. V. Ammosov, N. B. Delone, and V. P. Krainov, Zh. Eksp. Teor. Fiz. **91**, 2008 (1986) [Sov. Phys. JETP **64**, 1191 (1986)].
[15] M. Lewenstein, P. Balcou, M. Y. Ivanov, A. L'Huillier, and P. B. Corkum, Phys. Rev. A **49**, 2117 (1994).
[16] J. Tate, T. Auguste, H. G. Muller, P. Salières, P. Agostini, and L. F. DiMauro, Phys. Rev. Lett. **98**, 013901 (2007).
[17] S. P. Goreslavski, G. G. Paulus, S. V. Popruzhenko, and N. I. Shvetsov-Shilovski, Phys. Rev. Lett. **93**, 233002 (2004).
[18] A. S. Landsman, C. Hofmann, A. N. Pfeiffer, C. Cirelli, and U. Keller, Phys. Rev. Lett. **111**, 263001 (2013).
[19] T. Brabec, M. Y. Ivanov, and P. B. Corkum, Phys. Rev. A **54**, R2551 (1996).
[20] V. R. Bhardwaj, S. A. Aseyev, M. Mehendale, G. L. Yudin, D. M. Villeneuve, D. M. Rayner, M. Y. Ivanov, and P. B. Corkum, Phys. Rev. Lett. **86**, 3522 (2001).
[21] G. L. Yudin and M. Y. Ivanov, Phys. Rev. A **63**, 033404 (2001).
[22] L. B. Fu, J. Liu, J. Chen, and S.-G. Chen, Phys. Rev. A **63**, 043416 (2001).
[23] D. Comtois, D. Zeidler, H. Pépin, J. C. Kieffer, D. M. Villeneuve, and P. B. Corkum, J. Phys. B: At. Mol. Opt. Phys. **38**, 1923 (2005).
[24] J. Dubois, S. A. Berman, C. Chandre, and T. Uzer, Phys. Rev. Lett. **121**, 113202 (2018).
[25] J. Dubois, S. A. Berman, C. Chandre, and T. Uzer, Phys. Rev. E **98**, 052219 (2018).
[26] S. A. Berman, C. Chandre, and T. Uzer, Phys. Rev. A **92**, 023422 (2015).
[27] M. Li, M.-M. Liu, J.-W. Geng, M. Han, X. Sun, Y. Shao, Y. Deng, C. Wu, L.-Y. Peng, Q. Gong, and Y. Liu, Phys. Rev. A **95**, 053425 (2017).
[28] T. Nubbemeyer, K. Gorling, A. Saenz, U. Eichmann, and W. Sandner, Phys. Rev. Lett. **101**, 233001 (2008).
[29] J. Javanainen, J. H. Eberly, and Q. Su, Phys. Rev. A **38**, 3430 (1988).
[30] A. M. Perelomov, V. S. Popov, and M. V. Terent'ev, Zh. Eksp. Teor. Fiz. **50**, 1393 (1966) [Sov. Phys. JETP **23**, 924 (1966)].
[31] A. M. Perelomov, V. S. Popov, and M. V. Terent'ev, Zh. Eksp. Teor. Fiz. **51**, 309 (1967) [Sov. Phys. JETP **24**, 207 (1967)].
[32] A. M. Perelomov and V. S. Popov, Zh. Eksp. Teor. Fiz. **52**, 514 (1967) [Sov. Phys. JETP **25**, 336 (1967)].
[33] M. Klaiber, K. Z. Hatsagortsyan, and C. H. Keitel, Phys. Rev. Lett. **114**, 083001 (2015).
[34] S. V. Popruzhenko and D. Bauer, J. Mod. Opt. **55**, 2573 (2008).
[35] S. V. Popruzhenko, G. G. Paulus, and D. Bauer, Phys. Rev. A **77**, 053409 (2008).
[36] S. V. Popruzhenko, V. D. Mur, V. S. Popov, and D. Bauer, Phys. Rev. Lett. **101**, 193003 (2008).
[37] A. Kästner, U. Saalmann, and J. M. Rost, Phys. Rev. Lett. **108**, 033201 (2012).
[38] A. Kamor, C. Chandre, T. Uzer, and F. Mauger, Phys. Rev. Lett. **112**, 133003 (2014).
[39] S. A. Kelvich, W. Becker, and S. P. Goreslavski, Phys. Rev. A **93**, 033411 (2016).
[40] S. A. Kelvich, W. Becker, and S. P. Goreslavski, Phys. Rev. A **96**, 023427 (2017).
[41] V. D. Mur, S. V. Popruzhenko, and V. S. Popov, JETP **92**, 777 (2001).
[42] L. Torlina, F. Morales, J. Kaushal, I. Ivanov, A. Kheifets, A. Zielinski, A. Scrinzi, H. G. Muller, S. Sukiasyan, M. Ivanov, and O. Smirnova, Nat. Phys. **11**, 503 (2015).
[43] J. Liu, Y. Fu, W. Chen, Z. Lu, J. Zhao, J. Yuan, and Z. Zhao, J. Phys. B **50**, 055602 (2017).
[44] A. Rudenko, K. Zrost, T. Ergler, A. B. Voitkiv, B. Najjari, V. L. B. de Jesus, B. Feuerstein, C. D. Schröter, R. Moshammer, and J. Ullrich, J. Phys. B: At. Mol. Opt. Phys. **38**, L191 (2005).
[45] Q. Z. Xia, D. F. Ye, L. B. Fu, X. Y. Han, and J. Liu, Sci. Rep. **5**, 11473 (2015).
[46] M. Murakami and S.-I. Chu, Phys. Rev. A **93**, 023425 (2016).
[47] C. I. Blaga, F. Catoire, P. Colosimo, G. G. Paulus, H. G. Muller, P. Agostini, and L. F. DiMauro, Nat. Phys. **5**, 335 (2009).
[48] J. Maurer, B. Willenberg, J. Danek, B. W. Mayer, C. R. Phillips, L. Gallmann, M. Klaiber, K. Z. Hatsagortsyan, C. H. Keitel, and U. Keller, Phys. Rev. A **97**, 013404 (2018).
[49] A. S. Landsman, A. N. Pfeiffer, C. Hofmann, M. Smolarski, C. Cirelli, and U. Keller, New J. Phys. **15**, 013001 (2013).
[50] J. Daněk, M. Klaiber, K. Z. Hatsagortsyan, C. H. Keitel, B. Willenberg, J. Maurer, B. W. Mayer, C. R. Phillips, L. Gallmann, and U. Keller, J. Phys. B: At. Mol. Opt. Phys. **51**, 114001 (2018).
[51] M. Li, Y. Liu, H. Liu, Q. Ning, L. Fu, J. Liu, Y. Deng, C. Wu, L.-Y. Peng, and Q. Gong, Phys. Rev. Lett. **111**, 023006 (2013).
[52] D. P. Gurfil and P. K. Seidelmann, *Celestial Mechanics and Astrodynamics: Theory and Practice* (Springer Nature, Berlin, 2016), pp. 310–311.